



HAL
open science

Structural basis of CHMP2A–CHMP3 ESCRT-III polymer assembly and membrane cleavage

Kimi Azad, Delphine Guilligay, Cecile Boscheron, Sourav Maity, Nicola de Franceschi, Guidenn Sulbaran, Gregory Effantin, Haiyan Wang, Jean-Philippe Kleman, Patricia Bassereau, et al.

► **To cite this version:**

Kimi Azad, Delphine Guilligay, Cecile Boscheron, Sourav Maity, Nicola de Franceschi, et al.. Structural basis of CHMP2A–CHMP3 ESCRT-III polymer assembly and membrane cleavage. *Nature Structural and Molecular Biology*, 2023, 30 (1), pp.81-90. 10.1038/s41594-022-00867-8 . hal-03962316

HAL Id: hal-03962316

<https://hal.science/hal-03962316v1>

Submitted on 1 Feb 2023

HAL is a multi-disciplinary open access archive for the deposit and dissemination of scientific research documents, whether they are published or not. The documents may come from teaching and research institutions in France or abroad, or from public or private research centers.

L'archive ouverte pluridisciplinaire **HAL**, est destinée au dépôt et à la diffusion de documents scientifiques de niveau recherche, publiés ou non, émanant des établissements d'enseignement et de recherche français ou étrangers, des laboratoires publics ou privés.

28 **Abstract**

29 The endosomal sorting complex required for transport (ESCRT) is a highly conserved multi-protein
30 complex machinery that drives a diverse set of physiological and pathological membrane
31 remodeling processes. Membrane remodeling is essentially catalyzed by ESCRT-III filaments
32 adopting different geometries that stabilize either negatively or positively curved membranes¹.
33 The filaments are remodeled and ultimately recycled by the AAA-type ATPase VPS4, which sets
34 the stage for membrane fission²⁻⁴. However, the structural basis of ESCRT-III polymers stabilizing,
35 constricting and cleaving negatively curved membranes is unknown. Here we reconstituted the
36 ESCRT-III CHMP2A and CHMP3 polymer within narrow membrane tubes. Cryo electron
37 microscopy structures of the membrane-coated CHMP2A-CHMP3 filaments of two different
38 diameters at 3.3 and 3.6 Å resolution, respectively, show helical filaments assembled by
39 CHMP2A-CHMP3 heterodimers in the open ESCRT-III conformation⁵. Polymerization via helical
40 hairpin stacking generates a partially positive charged membrane interaction surface, positions
41 short N-terminal motifs for membrane interaction and the C-terminal VPS4 target sequence
42 towards the tube interior. Inter-filament interactions are electrostatic, which facilitate filament
43 sliding upon VPS4-mediated polymer remodeling. Fluorescence microscopy as well as high speed
44 atomic force microscopy imaging corroborate that VPS4 and CHMP2A-CHMP3 polymers can
45 constrict and cleave narrow membrane tubes, thus acting as a minimal membrane fission
46 machinery resembling the ancestral ESCRT-III-VPS4 function.

47

48 **Main**

49 The endosomal sorting complex required for transport (ESCRT) machinery catalyzes
50 many divergent membrane remodeling processes including the formation of multivesicular
51 endosomes, cytokinesis, nuclear envelope reformation, membrane repair, autophagy, exosome
52 biogenesis, neuronal pruning, dendritic spine maintenance, enveloped virus budding, release of
53 peroxisomes and of recycling endosomes⁶⁻¹⁴. Common to all ESCRT-catalyzed processes in
54 eukaryotes, archaea and bacteria is the recruitment of ESCRT-III proteins that polymerize to
55 generate and/or to stabilize membranes with either flat, negatively or positively curved geometries
56^{1-3,15-19}. The principal function of the polymers is to induce membrane constriction via outside-in
57 fission of tubular structures or inside-out fission from within membrane neck structures^{1-4,20,21}.

58 Humans express eight ESCRT-III proteins that are in a closed conformation in the cytosol
59²²⁻²⁴. Membrane recruitment is thought to activate ESCRT-III entailing opening up of the small
60 helical assembly²⁵⁻²⁷, which leads to an extended polymer-competent open ESCRT-III
61 conformation^{5,28,29} that is conserved across all kingdoms of life¹⁷⁻¹⁹. While most of these structures

62 demonstrate filament formation to stabilize positively curved membranes^{5,17-19} only low resolution
63 models for filaments stabilizing negatively curved membranes have been imaged revealing single
64 and multi-stranded polymers *in vitro*^{15,16,23,30-36} and *in vivo*^{35,37-42}. Notably CHMP3 copolymerizes
65 with CHMP2A into helical tubular structures with constant diameters of +/- 50 nm *in vitro*^{30,43},
66 which are remodeled and cleaved in the absence of membrane by VPS4⁴⁴.

67 Many ESCRT processes act on negatively curved membranes to catalyze inside-out
68 membrane fission. Here, we determined the structural basis of a late acting ESCRT-III polymer
69 stabilizing negatively curved membranes by cryo electron microscopy, which shows how the
70 filaments can slide upon VPS4 remodeling to induce constriction and membrane fission.

71

72 **Structure of the CHMP2A-CHMP3 polymer assembled within membrane tubes**

73 CHMP3 full length (residues 1-222) and C-terminally truncated CHMP2A (residues 1-164) were
74 assembled into helical tubular structures as described³⁰. After removal of the N-terminal tags, the
75 tubular structures were coated with lipid bilayer, which tightly associated with the protein layer as
76 shown by cryo electron microscopy (cryo-EM) (**Extended Data Fig.1A**). 2D classification of the
77 manually picked tube-like structures generated a dataset composed of 5 different diameters
78 ranging from 380 Å to 490 Å, with the 410 Å (51.4%) and 430 Å (31.2%) diameters representing
79 the most populated classes (**Extended Data Fig.1B**). The power spectra of the segments of the
80 class averages of the two diameters (**Extended Data Fig. 1C and D**) were then employed to
81 explore possible helical symmetries and combined with helical real-space reconstruction⁴⁵ to
82 validate the symmetry parameters. This revealed that the 410 Å and 430 Å diameter tubes are
83 formed by elementary helices composed of respectively 6.3 and 6.6 units per turn with a small
84 pitch of 9 Å for the 410 Å diameter and 18 Å for the 430 Å diameter. The latter displays an
85 additional C2 symmetry around the helical axis, explaining the doubling of the pitch (**Extended**
86 **Data Fig.1C and D**). Although, the asymmetric units along the elementary helix are not
87 biochemically connected, they translate into filaments with extended interaction surfaces between
88 subsequent asymmetric units. The symmetry parameters of the filaments are relatively similar for
89 both diameters (Rise/Twist of 8.227 Å /16.877° and 8.641 Å /17.701° for the 410 Å and 430 Å
90 diameters, respectively), and therefore likely represent the preferred polymerization mode of the
91 repeating unit, the CHMP2A-CHMP3 heterodimers (**Extended Data Fig.1C and D**).

92 Six filaments (2*3 in the case of the C2 symmetric helix) form left-handed six-start helices
93 with helical pitches of ~175 Å for both diameters (**Figures 1A and B**). The 430 Å filament is
94 composed of 21.33 units per turn (**Figures 1A and B**) and the 410 Å filament contains 20.33 units
95 per turn (**Figures 1C and D**), indicating a helical repeat after three turns and similar inter-filament

96 interactions along the helical axis. Comparison of the 430 and 410 Å demonstrates that removal
97 of one heterodimer reduces the tube diameter by 20 Å.

98 The three-dimensional (3D) helical reconstruction shows an overall resolution of 3.6 Å for
99 the 410 Å and 3.3 Å for the 430 Å diameter (**Figure 1 and Extended Data Fig. 2**) with local
100 resolutions ranging from 3.3 Å to 4.6 Å for the 430 Å diameter and 3.6 to 5.2 for the 410 Å diameter
101 (**Extended Data Fig. S3A, B and C**). The map of the 430 Å diameter was employed (**Figure 1E**)
102 to build the atomic model of the repeating unit of the filament, formed by the CHMP2A-CHMP3
103 heterodimer revealing both protomers in the open ESCRT-III conformation (**Figure**
104 **1F, Extended Data Fig. 3D, Extended Data Table 1**).

105 Comparison of the closed^{22,23} and open CHMP3 conformations showed the conformational
106 transitions upon CHMP3 activation, which involves extension of the helical hairpin (residues P12-
107 A101) that is identical in both conformations (r.m.s.d. of 1.082 Å) by a linker and helix 3 (L117).
108 The following short connection forms an elbow and translates helix 4 by ~10 Å positioning helix 4
109 in a 140° angle with respect to the hairpin axis. Helix 4 is composed of the closed conformation
110 helix 4 and most of the disordered linker connecting to helix 5 via a 90° kink at positions M151 to
111 D152 (**Figure 2A**). The remaining CHMP3 residues 170 to 220 are flexible and disordered in the
112 structure. Both CHMP3 and CHMP2A open conformations are similar as superposition of their C α
113 atoms revealed an r.m.s.d. of 0.934 Å (**Extended Data Fig.4A**), suggesting that CHMP2A can
114 fold into the same closed conformation structure as CHMP3.

115 The repeating unit of the filament is the CHMP2A-CHMP3 heterodimer formed by parallel
116 interaction of their hairpins with the CHMP2A hairpin tip shifted by six helical turns with respect to
117 CHMP3 (**Figure 2B**). The heterodimer interaction covers 2026 Å² of CHMP2A and 1997 Å² of
118 CHMP3 surfaces involving 55 and 51 interface residues, respectively. The structure of the
119 heterodimer was further confirmed by mutagenesis. Introducing pairs of cysteine demonstrated
120 that CHMP2A_D57C together with CHMP3_S75C and CHMP2A_N18C together with
121 CHMP3_V110C (**Extended Data Fig.5A**) assembled into disulfide-linked heterodimers upon
122 polymerization into tube-like structures as shown by SDS-PAGE analyses and negative staining
123 EM (**Extended Data Fig.5B and C**). Furthermore, mutagenesis of CHMP2A-CHMP3 interface
124 residues (**Extended Data Fig.5D**) prevented polymerization as expected (**Extended Data**
125 **Fig.5E**). The principle of the heterodimer hairpin stacking is employed to assemble the filament,
126 which is further stabilized by lateral interactions of CHMP3_i elbow helix 4 with CHMP2A_i,
127 CHMP3_{i+1} and CHMP2A_{i+1}. In addition, CHMP3_i helix 5 interacts with the tip of the CHMP3_{i+2}
128 hairpin (**Figure 2B**), as observed in the closed conformation (**Figure 2A**)^{22,23}. Similar to CHMP3,
129 CHMP2A helix 4 exerts the same domain exchange interactions (**Figure 2B**). C α superposition of

130 the open CHMP3 conformation revealed the closest match with the *S. cerevisiae* Snf7 protomer
131 (**Extended Data Fig.4B**) and considerable differences with CHMP1B, Vipp1, PspA and Vps24^{5,17-}
132 ^{19,46} (**Extended Data Fig.4C-F**). Notably, different hairpin interactions and orientations of the
133 helical arms upon polymerization determine the filament geometry that leads to positively curved
134 membrane interaction by CHMP1B, Vipp1 and PspA^{5,17-19} underlining the extensive structural
135 plasticity of ESCRT-III proteins.

136 137 **CHMP2A-CHMP3 polymer interaction with membrane**

138 The CHMP2A-CHMP3 polymer is tightly associated with the lipid bilayer (**Extended Data Fig.1E**)
139 and both CHMP2A and CHMP3 expose the same regions to the membrane. The polymerization
140 mode positions the N-terminal regions of both CHMP2A and CHMP3 at the membrane interface.
141 Although CHMP3 residues 1-10 and CHMP2A residues 1- 7 are disordered, they are both oriented
142 by conserved prolines towards the lipid bilayer (**Figure 3A**) consistent with previous suggestions
143 that short amphipathic N-terminal helices insert into the bilayer^{38,47}. The main membrane
144 interaction surfaces locate to the elbow formed by helices 3 and 4 (residues K104 to R131)
145 exposing six basic residues of CHMP2A (K104, K108, R115, K118, K124, R131) and five basic
146 residues of CHMP3 (K106, K112, K119, K132, K136) prone to interact with negative charges of
147 the membrane (**Figure 3B**). The electrostatic potential map shows in addition to the stretch of
148 basic surfaces some negative and non-charged regions of the outer polymer surface (**Figure 3C**).
149 Most of the basic residues are conserved in *S. cerevisiae* Vps2 and Vps24 (**Extended Data**
150 **Fig.7A**). Notably, alanine mutagenesis of some CHMP3 basic residues within the membrane
151 interaction surface did not interfere with CHMP2A-CHMP3 polymerization *in vitro* (**Extended Data**
152 **Fig.6A**) nor did they affect the dominant negative effect of C-terminally truncated CHMP3 on VLP
153 release (**Extended Data Fig.6B**), indicating that membrane binding is complex and not only
154 electrostatic, consistent with plasma membrane localization of the CHMP3 mutant (**Extended**
155 **Data Fig.6C**).

156 157 **Inter-filament interactions**

158 Conserved basic helix 1 residues of CHMP2A and CHMP3 (**Extended Data Fig.7A**) are at the
159 filament interface opposed by a stretch of conserved acidic residues within helices 4 and 5
160 (**Extended Data Fig.7A**) of neighboring filaments (**Figure 3D**), which indicate electrostatic inter-
161 filament interactions (**Figure 3C**). Mutation of the helix 1 basic cluster within either CHMP2A or
162 CHMP3 prevented polymer formation *in vitro* (**Extended Data Fig.6D**), indicating that the basic
163 charge of helix 1 is important for filament polymerization, which is in line with mutagenesis of a

164 similar cluster of basic residues within helix 1 of CHMP3 abolishing its dominant negative effect
165 on HIV-1 budding ²². To further test the electrostatic inter-filament interactions, we exposed the
166 helical tubular CHMP2A-CHMP3 polymers to high ionic strength. This led to the partial unwinding
167 of the filaments producing single and multi-stranded filaments (**Extended Data Fig.8A-E**) in
168 agreement with the presence of single and multi-start helices upon CHMP2A-CHMP3
169 polymerization *in vitro* ⁴³. We suggest that these electrostatic interactions between filaments
170 enable filament sliding upon VPS4-catalyzed remodeling. The acidic cluster in helices 4 and 5 is
171 conserved in CHMP4A, B, C, CHMP5 and CHMP6 (**Extended Data Fig.7B**) indicating potential
172 similar involvement in inter-filament interaction for the formation of mixed filaments. Notably, the
173 acidic cluster is not conserved in CHMP1A and B, which stabilizes positively curved membranes
174 via basic charges present on the inside of the protein tube-like polymer ⁵. We therefore suggest
175 that the acidic cluster is a hallmark of ESCRT-III stabilizing negatively curved membrane
176 structures.

177

178 **VPS4 remodels and cleaves CHMP2A-CHMP3 membrane tubes**

179 We next tested whether VPS4B can remodel the CHMP2A-CHMP3 membrane coated tubes as
180 we have shown before for CHMP2A-CHMP3 tubes without membrane ⁴⁴. When we incubated
181 CHMP2-CHMP3 and VPS4B containing membrane tubes (**Extended Data Fig.9A**) with ATP and
182 Mg²⁺, complete disassembly of the tubes was observed (**Extended Data Fig.9B**). In order to
183 image tube remodeling by fluorescence microscopy, VPS4B and caged ATP were incorporated
184 into the tubes wrapped with fluorescently labelled membrane. Imaging of tubes containing either
185 only caged ATP (**Figures 4A and B; movie 1; Extended Data Fig.10A and B; movie 2**) or only
186 VPS4B (**Figures 4C and D; movie 3**) demonstrated that photolysis used to uncage ATP did not
187 affect the tube structure. However, tubes containing both caged ATP and VPS4B revealed
188 constriction and tube cleavage upon ATP activation at different sites starting at 30s leading to
189 complete disassembly within 270s (**Figure 4E and F; movie 4**) or starting at 69s (**Extended Data**
190 **Fig.10C and D; movie 5**) or 50 s (**movie 6**).

191 Tube cleavage was further confirmed by high-speed AFM (HS-AFM) imaging. First,
192 CHMP2A-CHMP3 tubes with and without membrane were imaged (**Extended Data Fig.11A-C**).
193 A comparative height histogram showed an increase in tube height of ~8 nm for the membrane
194 coated tubes (**Extended Data Fig.11D**), as expected for an unilamellar membrane coating. Next,
195 membrane-coated tubes loaded with 10 μM caged ATP with and without UV exposure (**Extended**
196 **Data Fig.11E; movie 7**) were recorded by HS-AFM. In the absence of VPS4B, photolysis of the
197 caged ATP did not induce changes in tube morphology, consistent with the observations using

198 fluorescence microscopy. Further, no changes in tube morphology were observed without UV
199 exposure for an extended period of time of CHMP2A-CHMP3 tubes coated with membrane and
200 loaded with VPS4B and caged ATP (**Figure 5A, movie 8**). However, upon UV exposure,
201 constriction and cleavage of the membrane coated tubes was observed (**Figure 5B; movie 9**).
202 Kymographs along the tube cross section (**Figure 5C**) and the evolution of the height at the
203 constriction sites over time (**Figure 5D**) reveal that complete cleavage of the membrane tube
204 occurs within a time period of ~ 200 s of UV exposure. We conclude that VPS4B can constrict the
205 CHMP2A-CHMP3 filaments bound to membranes that leads to membrane cleavage, reminiscent
206 of membrane fission.

207

208 **Discussion**

209 The structure of the CHMP2A-CHMP3 heteropolymer demonstrates how ESCRT-III
210 filaments polymerize into rigid structures that can stabilize and/or shape negatively curved
211 membrane necks with diameters of approximately 50 nm. Such membrane structures are present
212 at many ESCRT-catalyzed processes including vesicle and virus budding or at later stages during
213 cytokinetic midbody constriction^{2,48}. Although the structural principles of the open ESCRT-III
214 conformation are highly conserved between CHMP2A/CHMP3 and CHMP1B⁵, Snf7/Shrub
215 (CHMP4)^{28,29} and bacterial PspA and Vipp1¹⁷⁻¹⁹, differences in helical hairpin stacking and
216 orientations of the helical arms dictates the geometry of the filaments that stabilize positively
217 curved membrane or negatively curved membrane as in case of CHMP2A-CHMP3 polymerization.
218 Furthermore, assembly modes of ESCRT-III monomers can vary as shown for CHMP2A, CHMP3
219 and CHMP4B, which can yet adapt another filament geometry that stabilizes positively curved
220 membranes^{15,16}. Thus the plastic nature of ESCRT-III protein conformations can lead to variable
221 ESCRT-III filament geometries that can adapt a wide range of curvatures to accommodate ESCRT
222 function in different membrane remodeling processes¹.

223 A striking feature of the CHMP2A-CHMP3 polymer is the narrow range of tube diameters,
224 which is consistent with their late recruitment to catalyze last steps in membrane constriction.
225 During MVB biogenesis, *S. cerevisiae* ESCRT-III assembles first Vps20/Snf7 (CHMP6/CHMP4)
226 which in turn recruits Vps24/Vps2 (CHMP3/CHMP2)⁴⁹, which were suggested to block Snf7
227 (CHMP4) polymerization by capping ESCRT-III assembly prior to recycling^{50,51}. Likewise, CHMP4
228 isoforms recruit CHMP3 and CHMP2A to HIV-1 budding sites⁵² consistent with live cell imaging
229 of Gag and ESCRT-III recruitment^{53,54}. The narrow range of diameters of the CHMP2A-CHMP3
230 polymer structure suggests that recruitment of CHMP3 and CHMP2A molds membrane necks into
231 approximately 40 to 50 nm diameters, which sets the stage for further constriction. Comparison of

232 the 410 and 430 Å wide structures shows that removal of only one CHMP2A-CHMP3 heterodimer
233 per turn reduces the tube diameter by 20 Å, indicating how a stepwise removal of heterodimers
234 can successively induce membrane constriction.

235 Another feature of the tubular polymer is that it can assemble from single or multi-stranded
236 filaments⁴³ the latter being the preferred assembly *in vitro*. Interaction between filaments is driven
237 by complementary positive and negative charges. However, surprisingly, high ionic strength did
238 not disassemble the tube into individual filaments but preserved the multi-strand architecture. The
239 17.5 nm width of the six-stranded helix present in the structure fits the 17 nm wide helices imaged
240 at the midbody⁴⁰, suggesting that such spirals contain six ESCRT-III filaments. Since inter-
241 filament interactions are electrostatic, different ESCRT-III filaments may contribute to the
242 formation of mixed multi-stranded filaments^{35,55}. In line, acidic residues within helix 4 and basic
243 residues within helix 1 have been implicated in *S. cerevisiae* Snf7-Vps24 interaction⁵⁶. Because
244 basic and acidic charges within these regions are conserved in CHMP6, CHMP4A, B, C, CHMP2B
245 and CHMP5, filaments thereof may also form side by side via homo- or hetero-filament assembly.
246 The loose electrostatic inter-filament interactions likely facilitate sliding of filaments upon ESCRT-
247 III filament remodeling by VPS4, which catalyzes filament constriction prior to complete
248 disassembly⁴⁴. Notably, dynamic VPS4-mediated turnover of ESCRT-III has been proposed in
249 different membrane remodeling processes^{35,57,58}.

250 CHMP2A-CHMP3 polymers have been suggested to interact with negatively charged
251 membranes⁵⁹⁻⁶¹, which is confirmed by the cluster of basic residues within the membrane
252 interaction surface. Furthermore, the structure indicates that short N-terminal hydrophobic motifs,
253 implicated in ESCRT-III function^{38 47} are positioned to insert into the membrane. Although this N-
254 terminal motif is helical in a filament structure assembled by an intermediate Vps24 (CHMP3)
255 conformation⁴⁶, the corresponding helices of CHMP2A and CHMP3 are not visible in the
256 membrane-bound structure suggesting that the putative amphipathic helices can adopt different
257 membrane insertion angles. Polymer interaction with membrane is tight, which excludes other
258 membrane proteins thereby serving as a diffusion barrier⁶¹.

259 CHMP3 is dispensable for HIV-1 budding⁵² and *S. cerevisiae* Vps24 can be substituted
260 by Vps2 overexpression restoring partial endosomal cargo sorting⁶². Both processes depend on
261 CHMP2A and Vps2 interaction with CHMP4 or Snf7. The structure suggests that CHMP3 can be
262 structurally replaced by CHMP2A in the polymer, indicating that CHMP2A filaments on their own
263 may form similar helices. Although CHMP2A can polymerize into circular filaments with
264 approximate diameters of 40 nm that often coil up, no regular CHMP2A tube-like structures have
265 been yet imaged *in vitro*⁴³.

266 VPS4B remodels CHMP2A-CHMP3 helical tubular structures *in vitro*^{30,63} inducing filament
267 constriction and cleavage that generates dome-like end caps prior to complete disassembly, which
268 was proposed to drive membrane fission^{44,64}. Here, we show that VPS4B constricts and cleaves
269 CHMP2A-CHMP3 membrane-coated tubes via membrane fission likely via the formation of dome-
270 like end-caps⁴⁴. Cleavage of membrane tubes pulled from GUVs has been reported previously
271 by employing a minimal system composed of *S. cerevisiae* Snf7, Vps24, Vps2 and Vps4⁶⁵, while
272 another model proposed sequential recruitment of *S. cerevisiae* Snf7, followed by Vps2-Vps24,
273 Vps2-Did2 and Did2-Ist1 for final constriction⁵⁵. Our data suggests that CHMP2A-CHMP3
274 filaments constitute together with VPS4 a minimal ESCRT-III membrane fission machinery that
275 can constrict membrane necks with 40 to 50 nm large diameters to the point of fission. *In vivo*,
276 CHMP2A and CHMP3 are recruited by CHMP4 polymers, which nucleate CHMP2A-CHMP3
277 polymerization^{50,52}. It is yet unclear how many helical turns are required for constriction *in vivo*,
278 although more than one, as estimated from imaging⁵⁸, would allow filament sliding powered by
279 ATP-driven forces that can drive filament-induced membrane constriction and cleavage. Finally,
280 catalyzing membrane fission with a minimal machinery is well in line with ancestral ESCRT-III
281 function^{66,67}.

282

283

284 **Methods**

285

286 **Expression and purification**

287 CHMP2A Δ C containing residues 1 to 161 was subcloned in a pMAL-c5X vector with an additional
288 TEV site at the amino terminal end expressed as a MBP fusion protein in the C41 (DE3) *E. coli*
289 bacterial strain (Lucigen). Expression was induced for 1h at 37°C. Bacteria were lysed by
290 sonication in a buffer containing 50 mM HEPES pH 7.5, 300 mM NaCl, 1 mM DTT, 5 mM EDTA
291 and protease inhibitors. Cleared lysate was applied onto an amylose resin (New England Biolabs),
292 washed with buffer A (25mM HEPES 7.5, 150 mM NaCl, 1mM DTT), then with Buffer B (25 mM
293 HEPES pH 7.5, 1 M NaCl, 1 M KCl, 1mM DTT) followed by a last wash with Buffer A. Finally,
294 protein was eluted with buffer C (25 mM HEPES 7.5, 150 mM NaCl, 10 mM maltose). The most
295 concentrated fraction was directly applied to size exclusion chromatography (SEC) Superdex 200
296 column (GE Healthcare) in buffer D (25 mM HEPES pH 7.5, 150 mM NaCl).

297 Full-length CHMP3 was subcloned in a pProEX-HTb vector (Life Technologies, Thermo Fisher)
298 and expressed in BL21Gold (DE3) *E. coli* bacterial strain (Agilent). Expression was induced for 3h
299 at 37°C and purified as described³⁰ with minor modifications. Bacteria were lysed by sonication

300 in buffer E (25 mM HEPES pH 7.5, 150 mM NaCl, 10mM imidazole) containing protease inhibitors
301 and the cleared lysate was applied onto a Ni²⁺-chelating sepharose (Cytivia), washed extensively
302 with lysis buffer E, and subsequently with buffer F (25 mM HEPES pH 7.5, 300 mM NaCl, 300 mM
303 KCl, 20 mM imidazole) and buffer G (25 mM HEPES pH 7.5, 300 mM NaCl, 300 mM KCl, 50 mM
304 imidazole). Finally, CHMP3 was eluted with buffer H (25 mM HEPES 7.5, 150 mM NaCl, 350 mM
305 imidazole) and cleaved overnight at 4°C with Tobacco Etch Virus (TEV) protease at 1:100 (w/w)
306 ratio in the presence of 10 mM β-mercaptoethanol. Cleaved protein was then applied on a second
307 Ni²⁺-chelating sepharose in order to remove TEV, the His-tag and uncleaved protein. The final
308 step included size exclusion chromatography (SEC) on a Superdex 75 column (GE Healthcare)
309 in buffer D. CHMP3 concentrated at 300 μM was frozen for further use.

310 CHMP2AΔC-mutants containing residues 9 to 161 and CHMP3-mutants containing residues 9 to
311 183 were synthesized (ThermoFisher), subcloned in a pETM40 vector (PEPcore facility-EMBL
312 Heidelberg) and the pProEX-HTb (ThermoFisher) vector, respectively. Mutants were expressed
313 and purified as described above for wild type sequences.

314

315 **CHMP2A-CHMP3 membrane tube generation**

316 For helical tube formation as described previously³⁰, 10 μM CHMP2AΔC was mixed with 20 μM
317 full-length CHMP3 and incubated for 48-72h at 4°C. After incubation, tubes were harvested by
318 centrifugation at 20,000g for 30min and the pellet containing CHMP2AΔC-CHMP3 tubes was
319 resuspended in buffer D. In order to wrap the CHMP2AΔC-CHMP3 tubes with a lipid bilayer, the
320 following lipid film was produced containing 70% Egg phosphatidyl choline (Egg PC), 10% dioleoyl
321 glycerol phosphoserine (DOPS), 10% dioleoyl glycerol phosphoethanolamine (DOPE), 10% brain
322 phosphatidylinositol-4,5-bisphosphate (PI(4,5)P₂) and 2μL of dioleoyl-sn-glycero-3-
323 phosphoethanolamine-N-(lissamine rhodamine B sulfonyl) (LISS-Rhodamin PE) (all Avanti Polar
324 lipids). The lipid film was resuspended in water at a final concentration of 5 mg/mL. The
325 CHMP2AΔC-CHMP3 tubes (25 μL) were mixed with 25 μL of 2% CHAPS, 25 μL of lipids and 0.1
326 mg/mL of TEV protease (to remove the MBP from CHMP2AΔC) and incubated at room
327 temperature for 2h. To remove free lipids/micelles and CHAPS, the tubes were dialyzed twice for
328 48-72h against buffer I (25mM Tris pH 7.4, 25 mM NaCl, 1 mM β-mercaptoethanol and 0.5 g of
329 Bio-Beads (Biorad). After dialysis, CHMP2AΔC-CHMP3 tubes wrapped with bilayer were
330 incubated with Bio-Beads overnight at 4°C and removed by centrifugation. The quality of the
331 bilayer wrapped CHMP2AΔC-CHMP3 tubes was assessed by negative staining EM prior to cryo
332 EM data collection, fluorescence microscopy imaging and HS-AFM analysis.

333 To test remodeling by VPS4, CHMP2A-CHMP3 tubes were incubated with 10 μ M VPS4B, 5 μ M
334 $MgCl_2$ and 5 μ M caged ATP (#A1048 Invitrogen) prior to membrane wrapping, following the
335 protocol described above. Because deposition of the membrane onto the CHMP2A-CHMP3
336 protein coat requires extensive dialysis, the final VPS4 concentration present within the tubes can
337 be only estimated from SDS-PAGE; however, the final concentration of caged ATP inserted into
338 the tubes cannot be determined.

339

340 **CHMP2A-CHMP3-VPS4 membrane tube imaging**

341 Epifluorescence video microscopy of CHMP2A-CHMP3 membrane tubes containing VPS4B and
342 caged ATP was performed using an Olympus IX83 optical microscope equipped with a UPFLN
343 100X O-2PH/1.3 objective and an ORCA-Flash4.0 Digital sCMOS camera (Hamamatsu). A 5 μ L
344 aliquot of ESCRT-III tube suspension was spread on a slide, covered with a glass coverslip (#1)
345 and sealed with twinstil speed 22 (Picodent, ref 13001002) for imaging. Caged-ATP was uncaged
346 using a 10s 10% 365-nm LED illumination (Figures 4 A-F and movies S1-4) or using at each time
347 point a 100ms 30% 365-nm LED illumination (Extended Data Fig.10 and movies S4 and S5).
348 ESCRT tubes were fluorescently imaged using a 550nm LED (10% with an exposure time of
349 100ms) at 1 frame/s. Images were acquired using the Volocity software package. Images were
350 analyzed, adjusted, and cropped using ImageJ software.

351

352 **HS-AFM analysis**

353 The AFM images were acquired in amplitude modulation tapping mode in liquid, using high-speed
354 atomic force microscopes (RIBM, Japan)^{44,68}. The HS-AFM imaging was performed using USC-
355 F1.2-k0.15 cantilevers (NanoWorld, Switzerland), an ultrashort cantilever with a nominal spring
356 constant of 0.15 N/m and a resonance frequency \approx 0.5 MHz. All HS-AFM recordings were done
357 at room temperature and in buffer D. Uncaging of the caged ATP was performed by directly
358 irradiating 365 nm UV light at the AFM sample stage using an optical fiber. The membrane coated
359 tubes were immobilized at the surface using streptavidin on top of a lipid bilayer (DOPC) on mica
360 containing 0.01% biotinylated lipid⁶⁹. HS-AFM images were analyzed using Igor Pro, and ImageJ
361 with additional home written plugins⁷⁰. Height measurements were performed on raw images after
362 tilt correction.

363

364 **Dominant negative effect CHMP150 wild type and mutants**

365 CHMP3 residues 1–150 wt or mutants were synthesized (ThermoFisher) and cloned into the
366 pEGFP-N1 vector using restriction sites *Xho*1- *Hind*III. To determine the effect of GFP-CHMP3

367 (1–150) on virus like particle (VLP) production upon HIV-1 Gag expression, 293T cells were seeded
368 into 10mm dishes and transfected 24 hr later using a Jetprime (Polyplus) technique. The cultures
369 were cotransfected with 0.5 µg of Rev-independent HIV-1 Gag construct and with 2 µg of either
370 pcDNA or wild type and mutant versions of GFP-CHMP3(1–150). Twenty-four hours post
371 transfection, VLPs released into the culture medium were pelleted through sucrose. HIV-1 Gag
372 proteins in VLPs and cell lysates were detected by Western blotting with a mouse anti-p24
373 antibody (183-H12-5C). For live cell imaging cells were seeded in glass bottomed µ-dishes and
374 co-transfected with 0.8 µg of Rev-independent HIV-1 Gag construct, 0.2 µg of Gag-mCherry ⁷¹
375 and with 1 µg of either wild type or mutant GFP-CHMP3(1–150). Live cell fluorescent protein
376 localization was analyzed by spinning disc confocal microscopy 24 hr post transfection in HeLa
377 cells.

378 379 **Cryo-EM sample preparation and data collection**

380 *Cryo-electron microscopy.* 3.5 µL of sample were applied to glow discharged (45s 30 mA) 1.2/1.3
381 Ultrafoil holey grids (Quantifoil Micro Tools GmbH, Germany) and they were plunged frozen in
382 liquid ethane with a Vitrobot Mark IV (Thermo Fisher Scientific) (100% humidity, temperature 20°C,
383 6 s blot time, blot force 0). The grids were pre-screened on the 200kV Glacios electron microscope
384 (Thermo Fischer Scientific) at the IBS (Grenoble) and data were collected at the beamline CM01
385 of the ESRF (Grenoble, France) ⁷² on a Titan Krios G3 (Thermo Fischer Scientific) at 300 kV
386 equipped with an energy filter (Bioquantum LS/967, Gatan Inc, USA) (slit width of 20 eV). 5028
387 movies were recorded automatically on a K2 summit direct detector (Gatan Inc., USA) with EPU
388 (Thermo Fisher Scientific) for a total exposure time of 5 s and 200 ms per frame resulting in 25
389 frame movies with a total dose of ~24 e⁻/Å². The magnification was 130,000x (1.052 Å/pixel at the
390 camera level). The defocus of the images was adjusted between -0.5 and -1.5 µm in 0.2 µm
391 steps. For the high ionic strength unwinding of the CHMP2A-CHMPA filament the same grid and
392 freezing conditions have been used as described above and images have been recorded on the
393 Glacios electron microscope using a K2 direct electron detector.

394 395 **EM image analysis and 3D reconstructions**

396 The workflow of the image analysis is shown in **Extended Data Fig.2**. Electron beam-induced
397 sample motion on the recorded movie frames was corrected using MotionCor2 ⁷³ and the contrast
398 transfer function (CTF) was estimated with CTFFIND4 ⁷⁴. 9,207 filaments were manually picked
399 from 5,027 micrographs using the EMAN2 program e2helixboxer.py ⁷⁵. All subsequent data
400 processing steps were carried out in RELION3 ^{76,77} unless mentioned otherwise. Initially, 89,122

401 overlapping segments were extracted with ~90% overlap between boxes of 768 x 768 pixels and
402 downsampled to a pixel size of 2.104 for initial classification steps. Several rounds of 2D
403 classification resulted in class averages that could be classified into 5 main different groups based
404 on the filament diameter, without membrane (380 Å diameter (7.4%), 410 Å diameter (51.4%),
405 430 Å diameter (31.2%), 470 Å diameter (1.9%) and 490 Å diameter (0.3%)). In order to
406 compensate for potential mis-assignment of diameters to the segments due to inaccuracies in 2D
407 classification, we assigned to each entire tube a diameter based on the class assignment of the
408 corresponding segments. If more than 80% of segments of a particular tube were belonging to
409 classes assigned to a particular diameter, this entire tube would be assigned this diameter for the
410 subsequent steps. After re-extraction of segments with ~95% overlap, another round of 2D
411 classification was performed with the for each diameter group. Most populated 2D classes with
412 filament diameter of 430 Å and 410 Å were chosen for further processing and analysis. For
413 determination of helical symmetry, the sum of power spectra from a smaller subset (1,904 and
414 3,993 segments from one 2D class each for 430 Å and 410 Å respectively) was calculated for both
415 filament groups. The resulting average power spectrum (**Extended Data Fig.1C and D**) was
416 analyzed for estimation of helical symmetry parameters using the web tool helixplorer
417 (<http://rico.ibs.fr/helixplorer/>). Based on a prior visual inspection of the PS, we made following
418 hypotheses: the layer line with a maximum seemingly on the meridian could be the helical rise or
419 the pitch (given the large diameter of the tube and possibilities that selected 2D class averages
420 contained a number of slightly out-of-plane tilted segments). Given those two hypotheses, and
421 allowing any cyclic symmetries, we explored possible helical symmetries matching the
422 experimental PS, giving a list of 20 and 15 symmetries to test for the 430 Å and 410 Å diameter
423 classes, respectively. Those symmetries were applied on the real-space 2D class-averages using
424 SPRING program `segclassreconstruct.py`⁷⁸ in order to generate initial models and narrowing down
425 possible symmetry solutions to 14 and 10, by discarding those giving aberrant density distribution.
426 Using those initial models, each of the remaining symmetry solutions was tested for 3D refinement
427 in RELION3, and the resulting maps inspected for high-resolution features such as clear
428 secondary structures, allowing to determine the helical parameters to be 18 Å pitch, 2.72 Å rise,
429 54.39° twist, 6.6 units/turn and C2 point symmetry for 430 Å, and 9 Å pitch, 1.43 Å rise, 57° twist,
430 6.3 units/turn and C1 point symmetry for 410 Å diameter filaments.

431 In order to select a more homogeneous subset of segments, we applied 3D classification and the
432 classes (containing 25,353 and 11,396 segments for diameters 430 and 410 Å) were chosen for
433 a final round of 3D auto-refine reconstruction that converged to a 2.74 Å rise and 54.37° twist for
434 430 Å, and 1.44 Å rise and 57.04° twist for 410 Å diameter filaments. Using soft protein-only

435 masks, the final resolutions were estimated at 3.3 Å and 3.6 Å for the 430 Å and 410 Å diameter
436 filaments, at the FSC (Fourier shell correlation) 0.143 cutoff criterion⁷⁹. The maps were sharpened
437 with b-factors of -96.57 Å² (430 Å) and -101.52 Å² (410 Å). Local resolution was estimated in
438 RELION3⁷⁶ and the density maps were rendered in UCSF Chimera⁸⁰. The statistics of the EM
439 map are summarized in **Extended Data Table 1**.

440

441 **Atomic modelling and validation**

442 The SWISS-MODEL⁸¹ server was used to create homology models of human CHMP3 and
443 CHMP2A, using the open conformation of CHMP1B (PDB ID 6TZ4) as a reference model. Helices
444 with residues 15-52, 57-117 and 120-151 for CHMP3 and 14-51, 56-116 and 119-150 for CHMP2A
445 were initially fit into the EM density as separate rigid bodies using Chimera and then adjusted in
446 Coot⁸². Further, the rest of the N-terminal and C-terminal residues, as well as the connecting loops
447 were manually built and adjusted in Coot. The CHMP2A-CHMP3 heterodimer model was then
448 expanded by helical symmetry in each direction in order to get 10 such dimers surrounding the
449 central dimer. Thus, a total of 11 helical symmetry-related dimers were again checked in Coot,
450 before applying the first round of real-space refinement in PHENIX⁸³ with non-crystallographic
451 symmetry (NCS) restraints. NCS, along with SS (secondary structure) restraints were then used
452 for a second round of real-space refinement. At last, the symmetry-related dimers were removed
453 and the central CHMP2A-CHMP3 dimer was saved as the final model. The statistics of the final
454 models were tabulated using MolProbity⁸⁴ and are summarized in **Extended Data Table 11** and
455 map versus atomic model FSC plots were computed in PHENIX⁸⁵. All structure figures were
456 generated with UCSF Chimera, ChimeraX⁸⁶ and PyMOL (W. Delano; The PyMOL Molecular
457 Graphics System, Version 1.8 Schrödinger, LLC, <http://www.pymol.org>). Sequence alignments
458 were performed with Clustal Omega⁸⁷ and ESPript⁸⁸.

459

460 **Data Availability**

461 CryoEM maps and models were deposited to the PDB and EMDB with the following codes:
462 membrane-bound CHMP2A-CHMP3, 430 Å diameter (PDB ID 7ZCG, EMD-14630) and
463 membrane-bound CHMP2A-CHMP3, 410 Å diameter (PDB ID 7ZCH, EMD-14631).

464

465 **Acknowledgement**

466 This research was funded by the ANR (ANR-14-CE09-0003-01; ANR-19-CE11-0002-02)(W.W.).
467 WW acknowledges support from the Institut Universitaire de France (IUF) and access to the
468 platforms of the Grenoble Instruct-ERIC center (IBS and ISBG; UAR 3518 CNRS-CEA-UGA-

469 EMBL) within the Grenoble Partnership for Structural Biology (PSB), with support from FRISBI
470 (ANR-10-INBS-05-02) and GRAL, a project of the University Grenoble Alpes graduate school
471 (Ecoles Universitaires de Recherche) CBH-EUR-GS (ANR-17-EURE-0003). The IBS electron
472 microscope facility is supported by the Auvergne-Rhône-Alpes Region, the Fondation pour la
473 Recherche Medicale (FRM), the FEDER/ERDF fund (European Regional Development Fund) and
474 the GIS-IBiSA (Infrastructures en Biologie, Sante et Agronomie). We acknowledge the provision
475 of in-house experimental time from the CM01 facility at the ESRF and we thank Leandro Estrozi
476 for extensive discussion and help with helical image analysis.

477
478 **Author contributions:** W.W. conceived the study, designed experiments, interpreted
479 experiments, supervised and received funding for the study. K.A. performed all cryo-EM data
480 analyses. N.D.F. established the membrane coating protocol. D.G. prepared wild type and mutant
481 CHMP2A-CHMP3 polymers for all analyses. G.S. performed negative staining EM analyses. C.B.
482 and J.P.K. performed fluorescence microscopy imaging and H.W. mutant analyses. S.M.
483 performed AFM analyses and W.H.R. supervised AFM analyses. G.E. and G.S. collected cryoEM
484 data and A.D. supervised all aspects of cryoEM data analyses, structure solution and
485 interpretation. W.W. wrote the paper with input from all authors.

486
487 **Competing interests:** The authors declare no competing interests.

488
489 **References**

490 1. Pfitzner, A. K., Moser von Filseck, J. & Roux, A. Principles of membrane remodeling by
491 dynamic ESCRT-III polymers. *Trends Cell Biol* **31**, 856-868 (2021).
492 2. McCullough, J., Frost, A. & Sundquist, W. I. Structures, Functions, and Dynamics of
493 ESCRT-III/Vps4 Membrane Remodeling and Fission Complexes. *Annu Rev Cell Dev Biol*
494 **34**, 85-109 (2018).
495 3. Caillat, C., Maity, S., Miguet, N., Roos, W. H. & Weissenhorn, W. The role of VPS4 in
496 ESCRT-III polymer remodeling. *Biochem Soc Trans* **47**, 441-448 (2019).
497 4. Remec Pavlin, M. & Hurley, J. H. The ESCRTs - converging on mechanism. *J Cell Sci*
498 **133**(2020).
499 5. McCullough, J., Clippinger, A. K., Talledge, N., Skowyra, M. L., Saunders, M. G. *et al.*
500 Structure and membrane remodeling activity of ESCRT-III helical polymers. *Science* **350**,
501 1548-1551 (2015).
502 6. Henne, W. M., Stenmark, H. & Emr, S. D. Molecular mechanisms of the membrane
503 sculpting ESCRT pathway. *Cold Spring Harb Perspect Biol* **5**(2013).
504 7. Votteler, J. & Sundquist, W. I. Virus budding and the ESCRT pathway. *Cell Host Microbe*
505 **14**, 232-241 (2013).
506 8. Allison, R., Lumb, J. H., Fassier, C., Connell, J. W., Ten Martin, D. *et al.* An ESCRT-spastin
507 interaction promotes fission of recycling tubules from the endosome. *J Cell Biol* **202**, 527-
508 543 (2013).

- 509 9. Loncle, N., Agromayor, M., Martin-Serrano, J. & Williams, D. W. An ESCRT module is
510 required for neuron pruning. *Sci Rep* **5**, 8461 (2015).
- 511 10. Olmos, Y. & Carlton, J. G. The ESCRT machinery: new roles at new holes. *Curr Opin Cell*
512 *Biol* **38**, 1-11 (2016).
- 513 11. Scourfield, E. J. & Martin-Serrano, J. Growing functions of the ESCRT machinery in cell
514 biology and viral replication. *Biochem Soc Trans* **45**, 613-634 (2017).
- 515 12. Sadoul, R., Laporte, M. H., Chassefeyre, R., Chi, K. I., Goldberg, Y. *et al.* The role of
516 ESCRT during development and functioning of the nervous system. *Semin Cell Dev Biol*
517 **74**, 40-49 (2018).
- 518 13. Mast, F. D., Herricks, T., Strehler, K. M., Miller, L. R., Saleem, R. A. *et al.* ESCRT-III is
519 required for scissioning new peroxisomes from the endoplasmic reticulum. *J Cell Biol*
520 (2018).
- 521 14. Zhen, Y., Radulovic, M., Vietri, M. & Stenmark, H. Sealing holes in cellular membranes.
522 *EMBO J* **40**, e106922 (2021).
- 523 15. Bertin, A., de Franceschi, N., de la Mora, E., Maity, S., Alqabandi, M. *et al.* Human ESCRT-
524 III polymers assemble on positively curved membranes and induce helical membrane tube
525 formation. *Nat Commun* **11**, 2663 (2020).
- 526 16. Moser von Filseck, J., Barberi, L., Talledge, N., Johnson, I. E., Frost, A. *et al.* Anisotropic
527 ESCRT-III architecture governs helical membrane tube formation. *Nat Commun* **11**, 1516
528 (2020).
- 529 17. Liu, J., Tassinari, M., Souza, D. P., Naskar, S., Noel, J. K. *et al.* Bacterial Vipp1 and PspA
530 are members of the ancient ESCRT-III membrane-remodeling superfamily. *Cell* **184**, 3660-
531 3673 e3618 (2021).
- 532 18. Junglas, B., Huber, S. T., Heidler, T., Schlosser, L., Mann, D. *et al.* PspA adopts an
533 ESCRT-III-like fold and remodels bacterial membranes. *Cell* **184**, 3674-3688 e3618
534 (2021).
- 535 19. Gupta, T. K., Klumpe, S., Gries, K., Heinz, S., Wietrzynski, W. *et al.* Structural basis for
536 VIPP1 oligomerization and maintenance of thylakoid membrane integrity. *Cell* **184**, 3643-
537 3659 e3623 (2021).
- 538 20. Nguyen, H. C., Talledge, N., McCullough, J., Sharma, A., Moss, F. R., 3rd *et al.* Membrane
539 constriction and thinning by sequential ESCRT-III polymerization. *Nat Struct Mol Biol* **27**,
540 392-399 (2020).
- 541 21. Harker-Kirschneck, L., Hafner, A. E., Yao, T., Vanhille-Campos, C., Jiang, X. *et al.* Physical
542 mechanisms of ESCRT-III-driven cell division. *Proc Natl Acad Sci U S A* **119**(2022).
- 543 22. Muziol, T., Pineda-Molina, E., Ravelli, R. B., Zamborlini, A., Usami, Y. *et al.* Structural basis
544 for budding by the ESCRT-III factor CHMP3. *Dev Cell* **10**, 821-830 (2006).
- 545 23. Bajorek, M., Schubert, H. L., McCullough, J., Langelier, C., Eckert, D. M. *et al.* Structural
546 basis for ESCRT-III protein autoinhibition. *Nat Struct Mol Biol* **16**, 754-762 (2009).
- 547 24. Xiao, J., Chen, X. W., Davies, B. A., Saltiel, A. R., Katzmann, D. J. *et al.* Structural basis
548 of Ist1 function and Ist1-Did2 interaction in the multivesicular body pathway and
549 cytokinesis. *Mol Biol Cell* **20**, 3514-3524 (2009).
- 550 25. Zamborlini, A., Usami, Y., Radoshitzky, S. R., Popova, E., Palu, G. *et al.* Release of
551 autoinhibition converts ESCRT-III components into potent inhibitors of HIV-1 budding. *Proc*
552 *Natl Acad Sci U S A* **103**, 19140-19145 (2006).
- 553 26. Shim, S., Kimpler, L. A. & Hanson, P. I. Structure/Function Analysis of Four Core ESCRT-
554 III Proteins Reveals Common Regulatory Role for Extreme C-Terminal Domain. *Traffic* **8**,
555 1068-1079 (2007).
- 556 27. Lata, S., Roessle, M., Solomons, J., Jamin, M., Gottlinger, H. G. *et al.* Structural basis for
557 autoinhibition of ESCRT-III CHMP3. *J Mol Biol* **378**, 818-827 (2008).
- 558 28. Tang, S., Henne, W. M., Borbat, P. P., Buchkovich, N. J., Freed, J. H. *et al.* Structural basis
559 for activation, assembly and membrane binding of ESCRT-III Snf7 filaments. *Elife* **4**(2015).

- 560 29. McMillan, B. J., Tibbe, C., Jeon, H., Drabek, A. A., Klein, T. *et al.* Electrostatic Interactions
561 between Elongated Monomers Drive Filamentation of Drosophila Shrub, a Metazoan
562 ESCRT-III Protein. *Cell Rep* **16**, 1211-1217 (2016).
- 563 30. Lata, S., Schoehn, G., Jain, A., Pires, R., Piehler, J. *et al.* Helical structures of ESCRT-III
564 are disassembled by VPS4. *Science* **321**, 1354-1357 (2008).
- 565 31. Pires, R., Hartlieb, B., Signor, L., Schoehn, G., Lata, S. *et al.* A crescent-shaped ALIX
566 dimer targets ESCRT-III CHMP4 filaments. *Structure* **17**, 843-856 (2009).
- 567 32. Moriscot, C., Gribaldo, S., Jault, J. M., Krupovic, M., Arnaud, J. *et al.* Crenarchaeal CdvA
568 forms double-helical filaments containing DNA and interacts with ESCRT-III-like CdvB.
569 *PLoS ONE* **6**, e21921 (2011).
- 570 33. Dobro, M. J., Samson, R. Y., Yu, Z., McCullough, J., Ding, H. J. *et al.* Electron
571 cryotomography of ESCRT assemblies and dividing Sulfolobus cells suggests that
572 spiraling filaments are involved in membrane scission. *Mol Biol Cell* **24**, 2319-2327 (2013).
- 573 34. Chiaruttini, N., Redondo-Morata, L., Colom, A., Humbert, F., Lenz, M. *et al.* Relaxation of
574 Loaded ESCRT-III Spiral Springs Drives Membrane Deformation. *Cell* **163**, 866-879
575 (2015).
- 576 35. Mierzwa, B. E., Chiaruttini, N., Redondo-Morata, L., von Filseck, J. M., Konig, J. *et al.*
577 Dynamic subunit turnover in ESCRT-III assemblies is regulated by Vps4 to mediate
578 membrane remodelling during cytokinesis. *Nat Cell Biol* **19**, 787-798 (2017).
- 579 36. Henne, W. M., Buchkovich, N. J., Zhao, Y. & Emr, S. D. The Endosomal Sorting Complex
580 ESCRT-II Mediates the Assembly and Architecture of ESCRT-III Helices. *Cell* **151**, 356-
581 371 (2012).
- 582 37. Hanson, P. I., Roth, R., Lin, Y. & Heuser, J. E. Plasma membrane deformation by circular
583 arrays of ESCRT-III protein filaments. *J Cell Biol.* **180(2)**, 389-402 (2008).
- 584 38. Bodon, G., Chassefeyre, R., Pernet-Gallay, K., Martinelli, N., Effantin, G. *et al.* Charged
585 Multivesicular Body Protein 2B (CHMP2B) of the Endosomal Sorting Complex Required
586 for Transport-III (ESCRT-III) Polymerizes into Helical Structures Deforming the Plasma
587 Membrane. *Journal of Biological Chemistry* **286**, 40276-40286 (2011).
- 588 39. Cashikar, A. G., Shim, S., Roth, R., Maldazys, M. R., Heuser, J. E. *et al.* Structure of
589 cellular ESCRT-III spirals and their relationship to HIV budding. *Elife*, e02184 (2014).
- 590 40. Guizetti, J., Schermelleh, L., Mantler, J., Maar, S., Poser, I. *et al.* Cortical Constriction
591 During Abscission Involves Helices of ESCRT-III-Dependent Filaments. *Science*
592 **331(6024)**, 1616-1620 (2011).
- 593 41. Sherman, S., Kirchenbuechler, D., Nachmias, D., Tamir, A., Werner, S. *et al.* Resolving
594 new ultrastructural features of cytokinetic abscission with soft-X-ray cryo-tomography. *Sci*
595 *Rep.* **6**, 27629(2016).
- 596 42. Goliand, I., Adar-Levor, S., Segal, I., Nachmias, D., Dadosh, T. *et al.* Resolving ESCRT-III
597 Spirals at the Intercellular Bridge of Dividing Cells Using 3D STORM. *Cell Rep* **24**, 1756-
598 1764 (2018).
- 599 43. Effantin, G., Dordor, A., Sandrin, V., Martinelli, N., Sundquist, W. I. *et al.* ESCRT-III
600 CHMP2A and CHMP3 form variable helical polymers in vitro and act synergistically during
601 HIV-1 budding. *Cell Microbiol* **15**, 213-226 (2013).
- 602 44. Maity, S., Caillat, C., Miguet, N., Sulbaran, G., Effantin, G. *et al.* VPS4 triggers constriction
603 and cleavage of ESCRT-III helical filaments. *Sci Adv* **5**, eaau7198 (2019).
- 604 45. He, S. & Scheres, S. H. W. Helical reconstruction in RELION. *J Struct Biol* **198**, 163-176
605 (2017).
- 606 46. Huber, S. T., Mostafavi, S., Mortensen, S. A. & Sachse, C. Structure and assembly of
607 ESCRT-III helical Vps24 filaments. *Sci Adv* **6**, eaba4897 (2020).
- 608 47. Buchkovich, N. J., Henne, W. M., Tang, S. & Emr, S. D. Essential N-terminal insertion motif
609 anchors the ESCRT-III filament during MVB vesicle formation. *Dev Cell* **27**, 201-214
610 (2013).

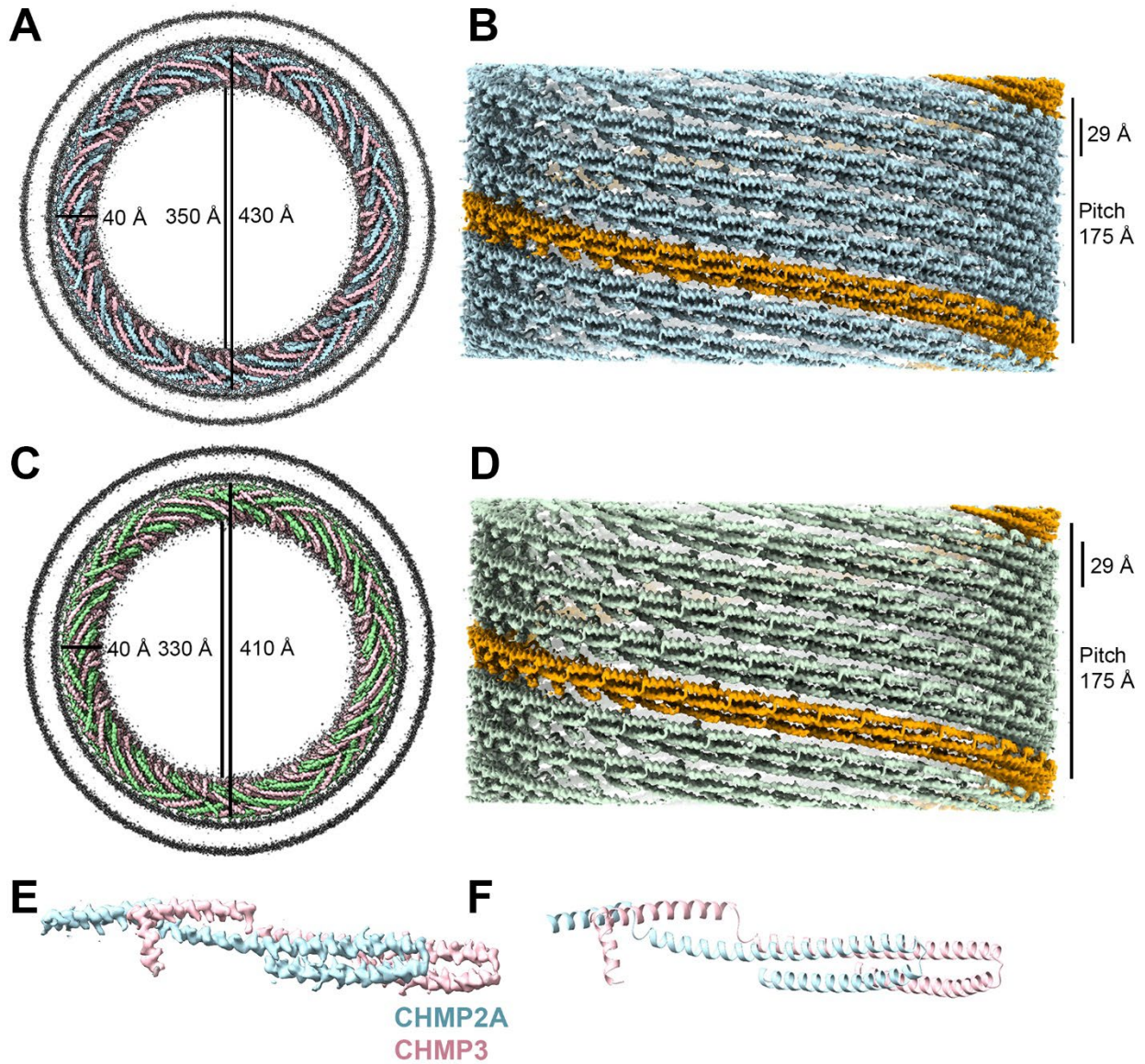
- 611 48. Vietri, M., Radulovic, M. & Stenmark, H. The many functions of ESCRTs. *Nat Rev Mol Cell Biol* **21**, 25-42 (2020).
- 612
- 613 49. Babst, M., Katzmann, D. J., Estepa-Sabal, E. J., Meerloo, T. & Emr, S. D. ESCRT-III: An
- 614 endosome-associated heterooligomeric protein complex required for MVB sorting. *Dev Cell* **3**, 271-282 (2002).
- 615
- 616 50. Teis, D., Saksena, S. & Emr, S. D. Ordered Assembly of the ESCRT-III Complex on
- 617 Endosomes Is Required to Sequester Cargo during MVB Formation. *Dev Cell* **15(4)**, 578-
- 618 589. (2008).
- 619 51. Saksena, S., Wahlman, J., Teis, D., Johnson, A. E. & Emr, S. D. Functional reconstitution
- 620 of ESCRT-III assembly and disassembly. *Cell* **136**, 97-109 (2009).
- 621 52. Morita, E., Sandrin, V., McCullough, J., Katsuyama, A., Baci Hamilton, I. *et al.* ESCRT-III
- 622 Protein Requirements for HIV-1 Budding. *Cell Host Microbe* **9**, 235-242 (2011).
- 623 53. Prescher, J., Baumgartel, V., Ivanchenko, S., Torrano, A. A., Brauchle, C. *et al.* Super-
- 624 resolution imaging of ESCRT-proteins at HIV-1 assembly sites. *PLoS Pathog* **11**,
- 625 e1004677 (2015).
- 626 54. Johnson, D. S., Bleck, M. & Simon, S. M. Timing of ESCRT-III protein recruitment and
- 627 membrane scission during HIV-1 assembly. *Elife* **7**(2018).
- 628 55. Pfitzner, A. K., Mercier, V., Jiang, X., Moser von Filseck, J., Baum, B. *et al.* An ESCRT-III
- 629 Polymerization Sequence Drives Membrane Deformation and Fission. *Cell* **182**, 1140-
- 630 1155 e1118 (2020).
- 631 56. Banjade, S., Tang, S., Shah, Y. H. & Emr, S. D. Electrostatic lateral interactions drive
- 632 ESCRT-III heteropolymer assembly. *Elife* **8**(2019).
- 633 57. Adell, M. A., Vogel, G. F., Pakdel, M., Muller, M., Lindner, H. *et al.* Coordinated binding of
- 634 Vps4 to ESCRT-III drives membrane neck constriction during MVB vesicle formation. *J Cell Biol* **205**,
- 635 33-49 (2014).
- 636 58. Adell, M. A. Y., Migliano, S. M., Upadhyayula, S., Bykov, Y. S., Sprenger, S. *et al.*
- 637 Recruitment dynamics of ESCRT-III and Vps4 to endosomes and implications for reverse
- 638 membrane budding. *Elife* **6**(2017).
- 639 59. Whitley, P., Reaves, B. J., Hashimoto, M., Riley, A. M., Potter, B. V. L. *et al.* Identification
- 640 of Mammalian Vps24p as an Effector of Phosphatidylinositol 3,5-Bisphosphate-dependent
- 641 Endosome Compartmentalization. *J. Biol. Chem.* **278**, 38786-38795 (2003).
- 642 60. Lin, Y., Kimpler, L. A., Naismith, T. V., Lauer, J. M. & Hanson, P. I. Interaction of the
- 643 mammalian endosomal sorting complex required for transport (ESCRT) III protein hSnf7-
- 644 1 with itself, membranes, and the AAA+ ATPase SKD1. *J. Biol. Chem.* **280**, 12799-12809
- 645 (2005).
- 646 61. De Franceschi, N., Alqabandi, M., Miguet, N., Caillat, C., Mangenot, S. *et al.* The ESCRT
- 647 protein CHMP2B acts as a diffusion barrier on reconstituted membrane necks. *J Cell Sci* **132**(2018).
- 648
- 649 62. Banjade, S., Shah, Y. H., Tang, S. & Emr, S. D. Design principles of the ESCRT-III Vps24-
- 650 Vps2 module. *Elife* **10**(2021).
- 651 63. Caillat, C., Macheboeuf, P., Wu, Y., McCarthy, A. A., Boeri-Erba, E. *et al.* Asymmetric ring
- 652 structure of Vps4 required for ESCRT-III disassembly. *Nat Commun* **6**, 8781 (2015).
- 653 64. Fabrikant, G., Lata, S., Riches, J. D., Briggs, J. A., Weissenhorn, W. *et al.* Computational
- 654 model of membrane fission catalyzed by ESCRT-III. *PLoS Comput Biol* **5**, e1000575
- 655 (2009).
- 656 65. Schoneberg, J., Pavlin, M. R., Yan, S., Righini, M., Lee, I. H. *et al.* ATP-dependent force
- 657 generation and membrane scission by ESCRT-III and Vps4. *Science* **362**, 1423-1428
- 658 (2018).
- 659 66. Caspi, Y. & Dekker, C. Dividing the Archaeal Way: The Ancient Cdv Cell-Division
- 660 Machinery. *Front Microbiol* **9**, 174 (2018).

- 661 67. Ithurbide, S., Gribaldo, S., Albers, S. V. & Pende, N. Spotlight on FtsZ-based cell division
662 in Archaea. *Trends Microbiol* (2022).
- 663 68. Maity, S., Ottele, J., Santiago, G. M., Frederix, P., Kroon, P. *et al.* Caught in the Act:
664 Mechanistic Insight into Supramolecular Polymerization-Driven Self-Replication from Real-
665 Time Visualization. *J Am Chem Soc* **142**, 13709-13717 (2020).
- 666 69. Keya, J. J., Inoue, D., Suzuki, Y., Kozai, T., Ishikuro, D. *et al.* High-Resolution Imaging of
667 a Single Gliding Protofilament of Tubulins by HS-AFM. *Sci Rep* **7**, 6166 (2017).
- 668 70. Maity, S., Trinco, G., Buzon, P., Anshari, Z. R., Kodera, N. *et al.* High-speed atomic force
669 microscopy reveals a three-state elevator mechanism in the citrate transporter CitS. *Proc*
670 *Natl Acad Sci U S A* **119**(2022).
- 671 71. Jouvenet, N., Bieniasz, P. D. & Simon, S. M. Imaging the biogenesis of individual HIV-1
672 virions in live cells. *Nature* **454**, 236-240 (2008).
- 673 72. Kandiah, E., Giraud, T., de Maria Antolinos, A., Dobias, F., Effantin, G. *et al.* CM01: a
674 facility for cryo-electron microscopy at the European Synchrotron. *Acta Crystallogr D Struct*
675 *Biol* **75**, 528-535 (2019).
- 676 73. Zheng, S. Q., Palovcak, E., Armache, J. P., Verba, K. A., Cheng, Y. *et al.* MotionCor2:
677 anisotropic correction of beam-induced motion for improved cryo-electron microscopy. *Nat*
678 *Methods* **14**, 331-332 (2017).
- 679 74. Rohou, A. & Grigorieff, N. CTFFIND4: Fast and accurate defocus estimation from electron
680 micrographs. *J Struct Biol* **192**, 216-221 (2015).
- 681 75. Tang, G., Peng, L., Baldwin, P. R., Mann, D. S., Jiang, W. *et al.* EMAN2: an extensible
682 image processing suite for electron microscopy. *J Struct Biol* **157**, 38-46 (2007).
- 683 76. Scheres, S. H. RELION: implementation of a Bayesian approach to cryo-EM structure
684 determination. *J Struct Biol* **180**, 519-530 (2012).
- 685 77. Zivanov, J., Nakane, T., Forsberg, B. O., Kimanius, D., Hagen, W. J. *et al.* New tools for
686 automated high-resolution cryo-EM structure determination in RELION-3. *Elife* **7**(2018).
- 687 78. Desfosses, A., Ciuffa, R., Gutsche, I. & Sachse, C. SPRING - an image processing
688 package for single-particle based helical reconstruction from electron cryomicrographs. *J*
689 *Struct Biol* **185**, 15-26 (2014).
- 690 79. Rosenthal, P. B. & Henderson, R. Optimal determination of particle orientation, absolute
691 hand, and contrast loss in single-particle electron cryomicroscopy. *J Mol Biol* **333**, 721-745
692 (2003).
- 693 80. Pettersen, E. F., Goddard, T. D., Huang, C. C., Couch, G. S., Greenblatt, D. M. *et al.* UCSF
694 Chimera--a visualization system for exploratory research and analysis. *J Comput Chem*
695 **25**, 1605-1612 (2004).
- 696 81. Waterhouse, A., Bertoni, M., Bienert, S., Studer, G., Tauriello, G. *et al.* SWISS-MODEL:
697 homology modelling of protein structures and complexes. *Nucleic Acids Res* **46**, W296-
698 W303 (2018).
- 699 82. Emsley, P., Lohkamp, B., Scott, W. G. & Cowtan, K. Features and development of Coot.
700 *Acta Crystallogr D Biol Crystallogr* **66**, 486-501 (2010).
- 701 83. Adams, P. D., Afonine, P. V., Bunkoczi, G., Chen, V. B., Davis, I. W. *et al.* PHENIX: a
702 comprehensive Python-based system for macromolecular structure solution. *Acta*
703 *Crystallogr D Biol Crystallogr* **66**, 213-221 (2010).
- 704 84. Williams, C. J., Headd, J. J., Moriarty, N. W., Prisant, M. G., Videau, L. L. *et al.* MolProbity:
705 More and better reference data for improved all-atom structure validation. *Protein Sci* **27**,
706 293-315 (2018).
- 707 85. Afonine, P. V., Poon, B. K., Read, R. J., Sobolev, O. V., Terwilliger, T. C. *et al.* Real-space
708 refinement in PHENIX for cryo-EM and crystallography. *Acta Crystallogr D Struct Biol* **74**,
709 531-544 (2018).

- 710 86. Goddard, T. D., Huang, C. C., Meng, E. C., Pettersen, E. F., Couch, G. S. *et al.* UCSF
711 ChimeraX: Meeting modern challenges in visualization and analysis. *Protein Sci* **27**, 14-25
712 (2018).
- 713 87. Goujon, M., McWilliam, H., Li, W., Valentin, F., Squizzato, S. *et al.* A new bioinformatics
714 analysis tools framework at EMBL-EBI. *Nucleic Acids Res* **38**, W695-699 (2010).
- 715 88. Robert, X. & Gouet, P. Deciphering key features in protein structures with the new
716 ENDscript server. *Nucleic Acids Res* **42**, W320-324 (2014).
- 717

718 **Figures**

719



720

721 **Figure 1: Cryo-EM structure of CHMP2A-CHMP3 membrane-coated helical polymers**

722 **(A)** Density map of the reconstructed 430 Å diameter CHMP2A-CHMP3 membrane tube with the
723 top view looking down the helical axis. The helical arrangement of CHMP2A (light blue) and
724 CHMP3 (pink) inside the bilayer membrane (dark grey) is shown. The thickness, and the inner
725 and outer diameter of the helical protein tube are also marked in Å.

726 **(B)** Side view of the helical polymer without the lipid membrane. One left-handed filament is
727 indicated in orange, and the thickness of one filament and the pitch of the helical assembly are
728 also marked.

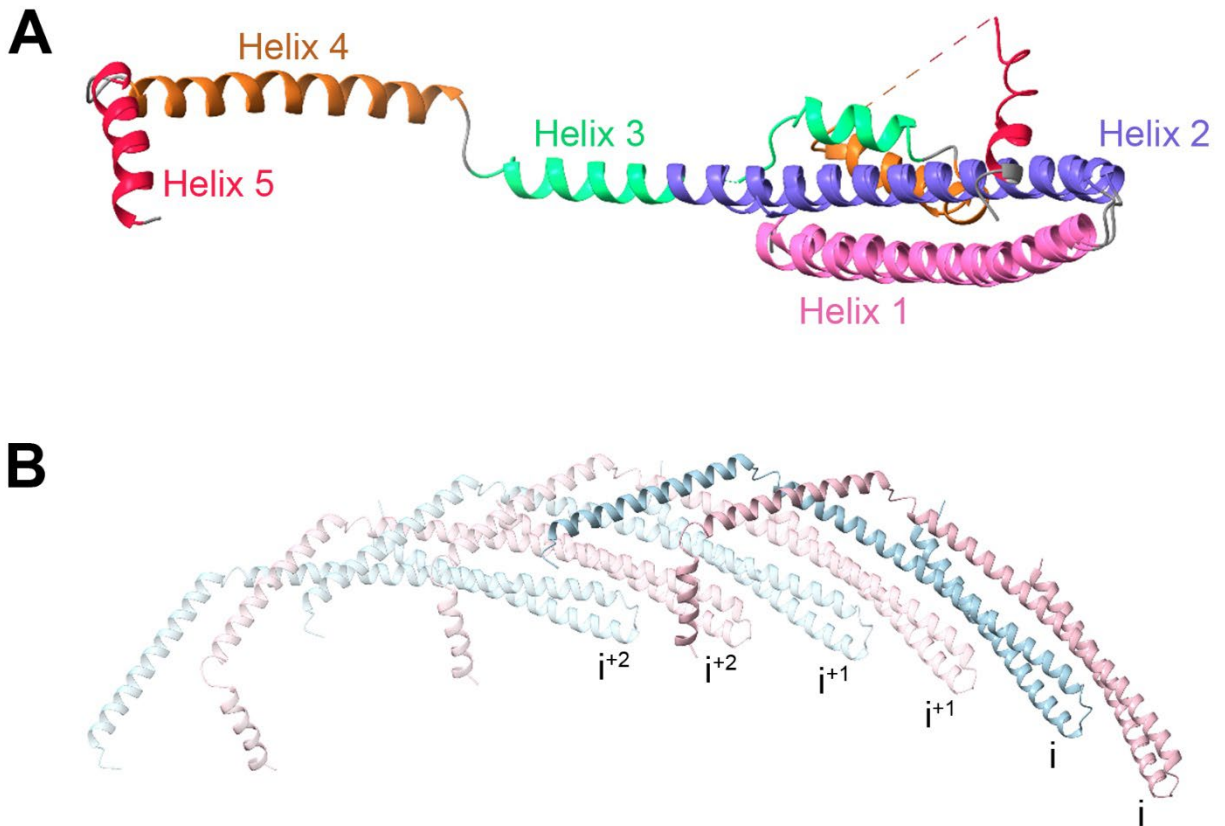
729 **(C)** Density map of the reconstructed 410 Å diameter CHMP2A-CHMP3 membrane tube with the
730 top view looking down the helical axis. The helical arrangement of CHMP2A (green) and CHMP3
731 (pink) inside the bilayer membrane (dark grey) is shown. The thickness, and the inner and outer
732 diameter of the helical protein tube are indicated in Å.

733 **(D)** Side view of the helical polymer without the lipid membrane. One left-handed filament is
734 indicated in orange, and the thickness of one filament and the pitch of the helical assembly are
735 indicated.

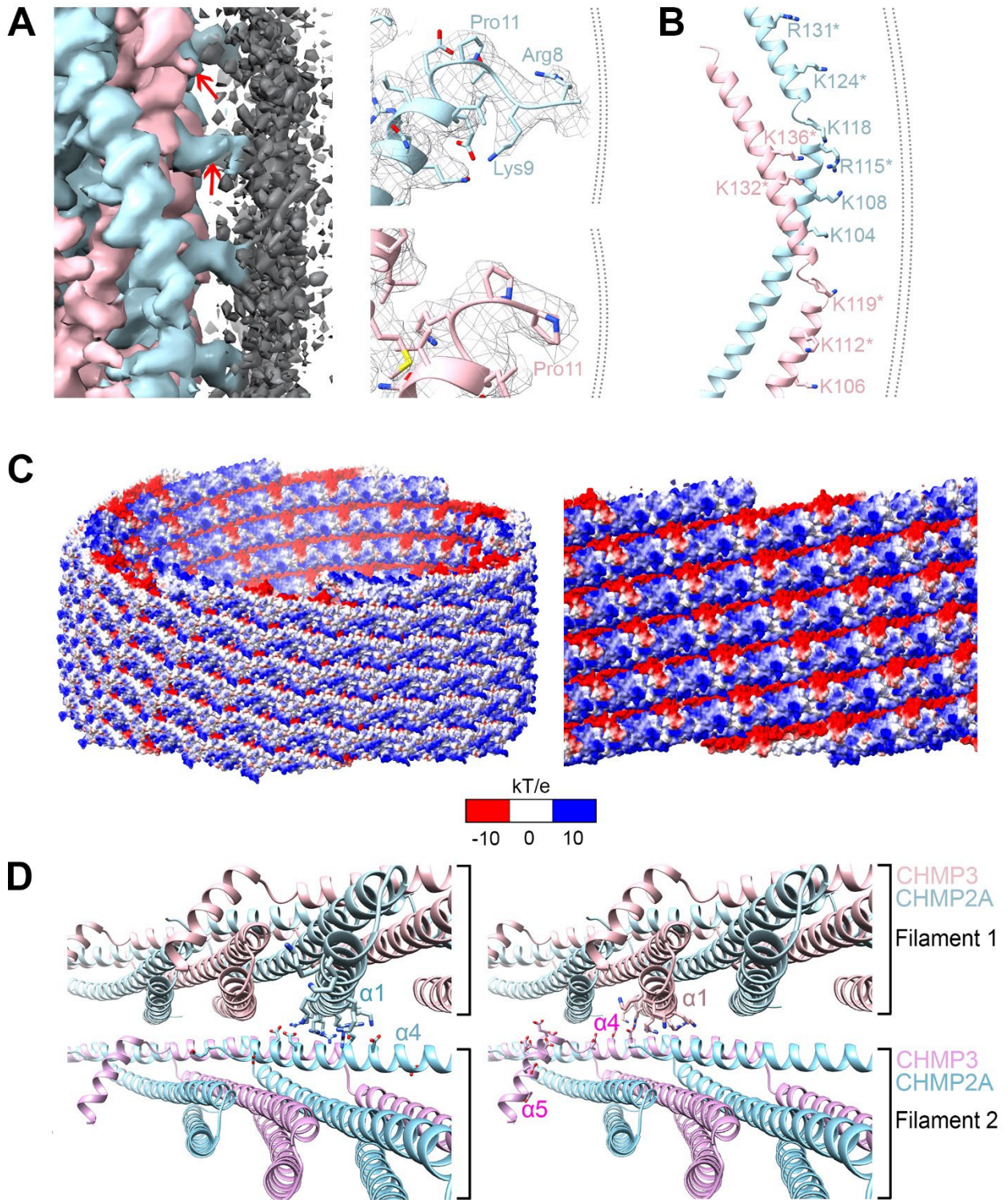
736 **(E)** Cryo-EM density of the single repeating unit of the 430 Å diameter polymer formed by the
737 heterodimer of CHMP2A (light blue) and CHMP3 (pink) is indicated.

738 **(F)** Ribbon representation of the atomic model of CHMP2A (light blue) - CHMP3 (pink)
739 heterodimer.

740



741
 742 **Figure 2: Atomic model and architecture of the CHMP2A-CHMP3 helical polymer.**
 743 **(A)** Ribbon diagram of Ca superposition of the closed and open CHMP3 conformations (Helix 1:
 744 pink, Helix 2: purple, Helix 3: light green, Helix 4: brown, Helix 5: red).
 745 **(B)** Three interlocked copies of CHMP2A-CHMP3 heterodimer are shown as ribbons. Helix 4 and
 746 5 of CHMP3 (pink) interact with four subsequent protomers. Helix 4 of CHMP2A (light blue) also
 747 makes similar interactions.
 748
 749



750

751

752 **Figure 3: Membrane interaction of the CHMP2A-CHMP3 filament.**

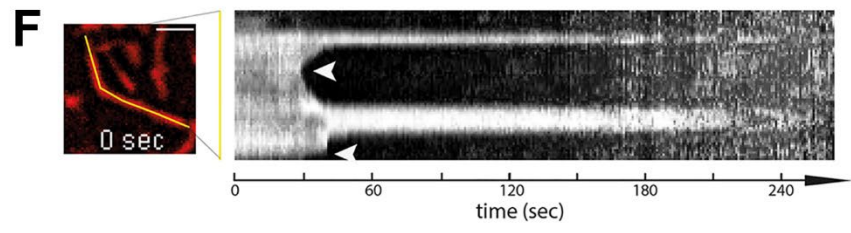
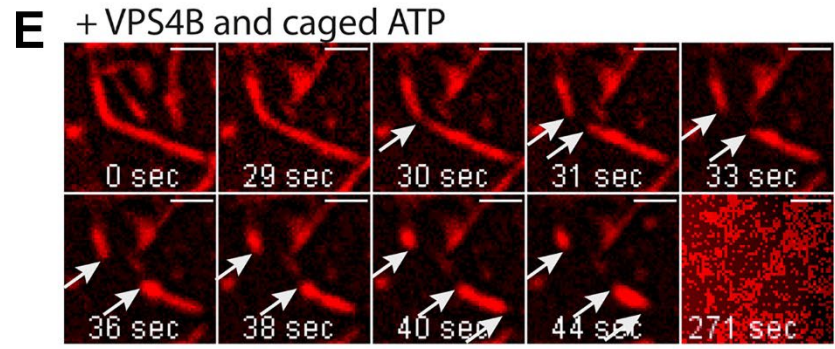
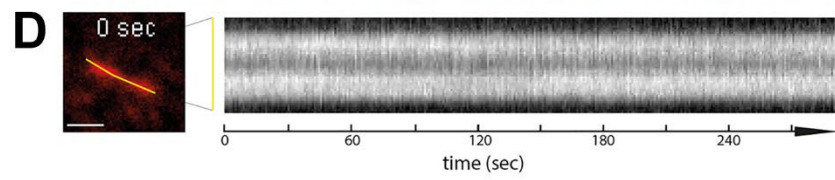
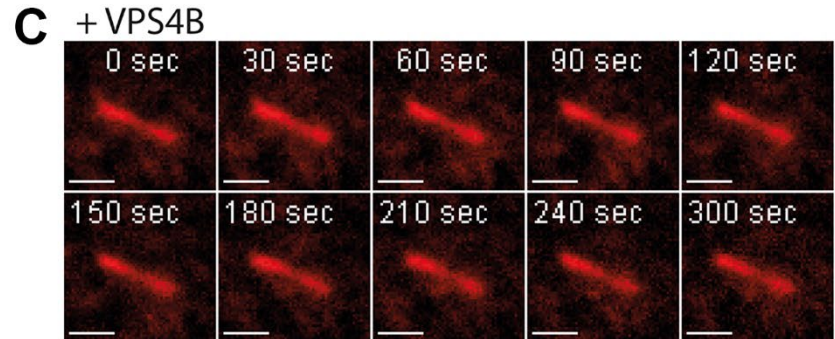
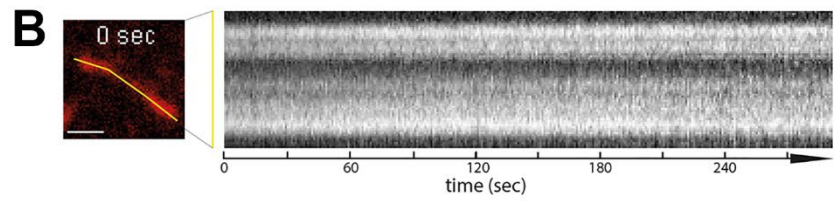
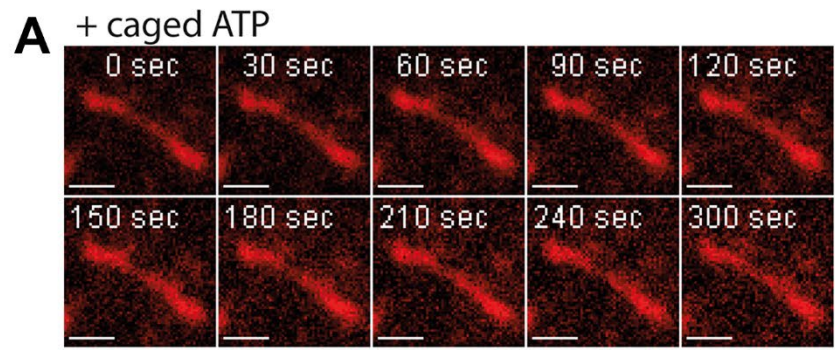
753 **(A)** Left panel, zoomed-in view of the membrane-bound CHMP2A-CHMP3 filament, highlighting
754 the interface between lipid membrane (dark grey) and CHMP2A (light blue) and CHMP3 (pink).
755 Red arrows are pointing to the N-termini of both CHMP2A and CHMP3 that are oriented towards
756 the lipid bilayer. Right panel, the orientation of the N-termini is determined by Pro11 of CHMP2A
757 (light blue) and CHMP3 (pink) shown with the density map.

758 **(B)** Ribbon diagram of the CHMP2A-CHMP3 heterodimer indicating the basic residues (sticks)
759 oriented towards the membrane. Basic residues conserved in yeast Vps2 and Vps24 are marked
760 by asterisks.

761 **(C)** Electrostatic potential map of the CHMP2A-CHMP3 filament (left panel, tilted, side view),
762 revealing the exposure of the cluster of basic charges, a small negatively charged surface and a
763 neutral surface to the membrane. Right panel, zoomed-in view of the electrostatic surface of the
764 inside of the polymer showing clusters of negative charges in one filament juxtaposed to positive
765 charges of the neighboring filament.

766 **(D)** Close-up of the inter-filament interactions. Ribbon diagram of two neighboring filaments
767 showing the basic and acidic residues of CHMP2A (left panel) and CHMP3 (right panel) implicated
768 in electrostatic inter-filament interactions.

769



771 **Figure 4: Imaging of VPS4B and ATP induced cleavage of CHMP2A-CHMP3 membrane**
772 **coated tubes.**

773 **(A)** A CHMP2A-CHMP3-caged ATP containing membrane coated tube was activated at 365 nm
774 (10%, 10s) to uncage ATP and imaged over 300s (movie S1).

775 **(B)** The kymograph of the tube shows that the tube stays intact over the imaging time.

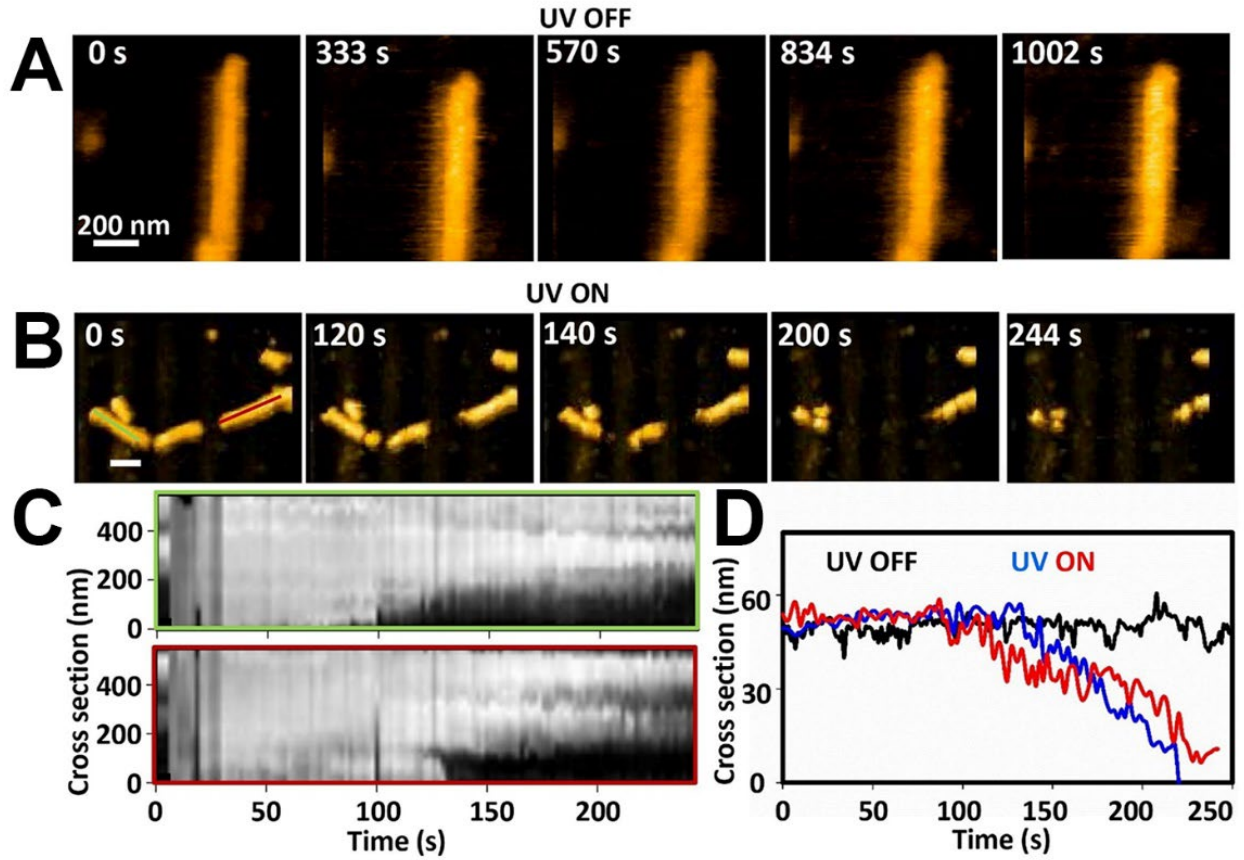
776 **(C)** A CHMP2A-CHMP3-VPS4B containing membrane coated tube was activated at 365 nm (10%,
777 10s) to uncage ATP and imaged over 300s.

778 **(D)** The kymograph of the tube shows that the tube stays intact over the imaging time. **(A)** to **(D)**
779 demonstrate that imaging at 550 nm to visualize the membrane tube and ATP uncaging at 365
780 nm did not change the tube structures (movie S2).

781 **(E)** Imaging of a CHMP2A-CHMP3-VPS4B-caged ATP containing membrane-coated tubes
782 following ATP uncaging (265 nm, 10%, 10s) reveals constriction and cleavage of the tube at 30
783 s followed by a shrinking event from both sides. Another shrinking event is observed at 40s.
784 Eventually all tubes were fully disassembled 271 s (movie S3 and S4). Bar, 1 μ m.

785 **(F)** The kymograph of the tube indicate the kinetics of cleavage and shrinking.

786



787
 788 **Figure 5. Constriction, cleavage, and disassembly of membrane coated CHMP2A-CHMP3**
 789 **tube.**

790 **(A)** Snapshots of HS-AFM images of CHMP2A-CHMP3 tubes coated with membrane and loaded
 791 with 5 μ M VPS4B, 10 mM caged ATP, in absence of UV irradiation. Scale bar 200 nm.

792 **(B)** As in A, but upon 365 nm UV irradiation. Scale bar 200 nm.

793 **(C)** Kymograph representation of the height vs time along the two lines in panel B (leftmost image)
 794 throughout the movie S10.

795 **(D)** Example of height vs time profile of the membrane coated tube in absence of UV irradiation
 796 (in black), and in presence of UV irradiation (in blue and red).

797

798
799
800
801

802
803
804
805
806
807
808
809
810
811
812

Supplementary data

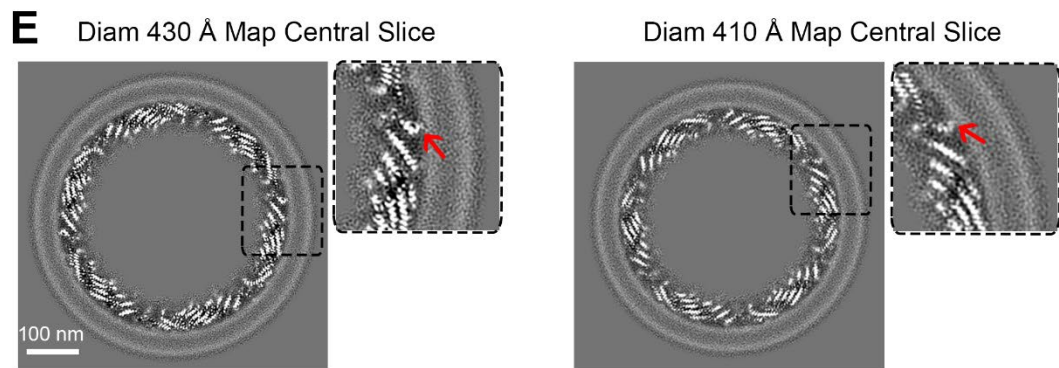
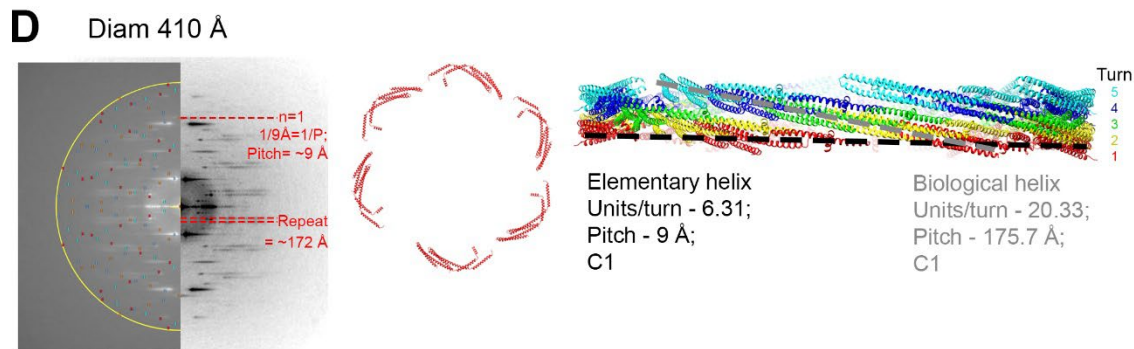
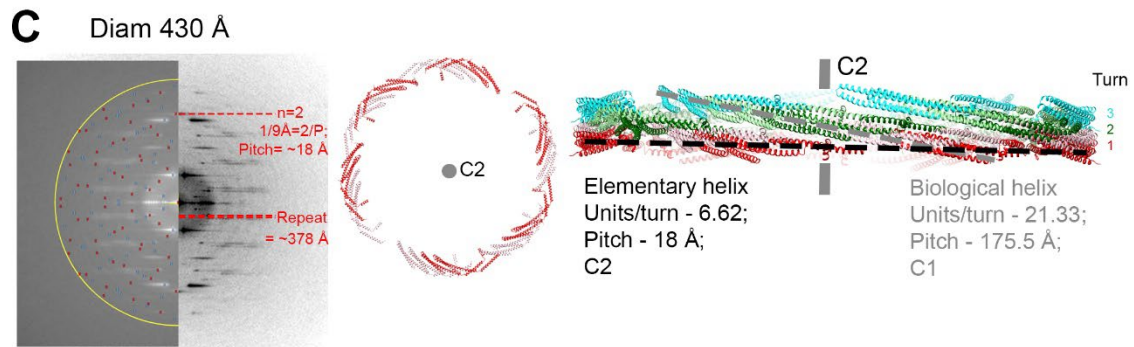
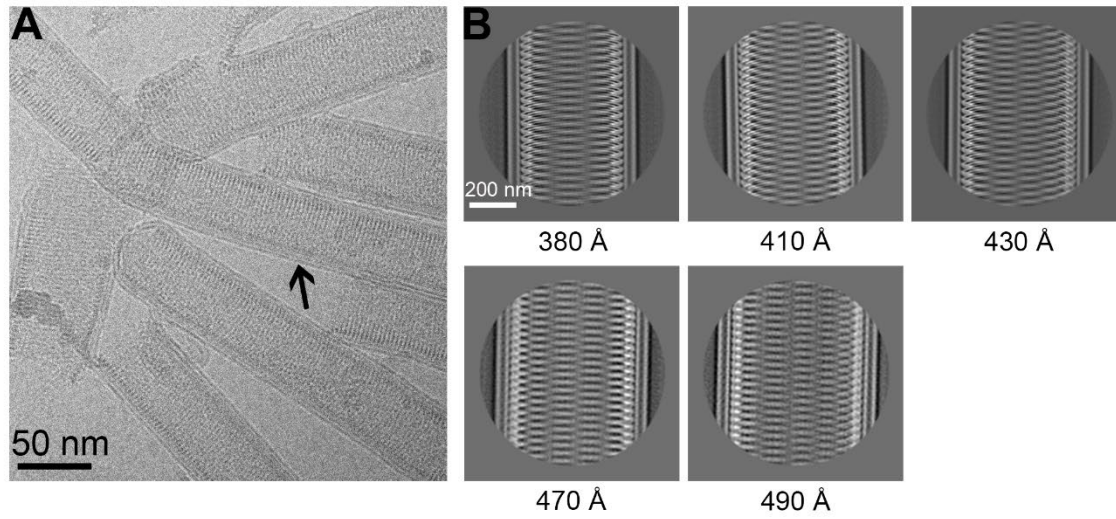
Structural basis of CHMP2A-CHMP3 ESCRT-III polymer assembly and membrane cleavage

Kimi Azad¹, Delphine Guilligay¹, Cecile Boscheron^{1*}, Sourav Maity^{2*}, Nicola De Franceschi^{1,3*},
Guidenn Sulbaran¹, Gregory Effantin¹, Haiyan Wang¹, Jean-Philippe Kleman¹, Patricia
Bassereau³, Guy Schoehn¹, Wouter H Roos², Ambroise Desfosses^{1*}, Winfried Weissenhorn^{1*}

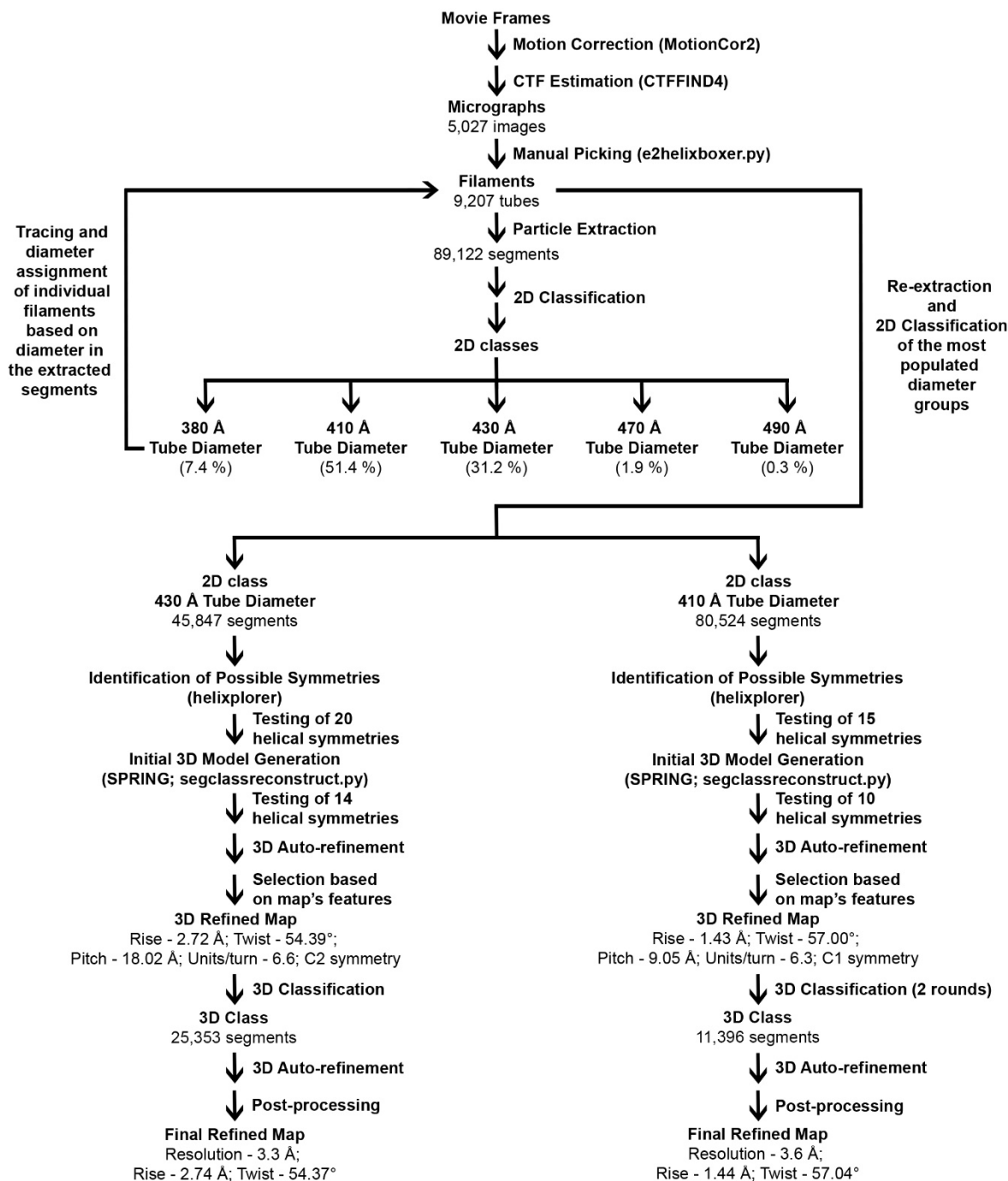
¹ Univ. Grenoble Alpes, CEA, CNRS, Institut de Biologie Structurale (IBS), Grenoble, France.

² Moleculaire Biofysica, Zernike Instituut, Rijksuniversiteit Groningen, Groningen, Netherlands.

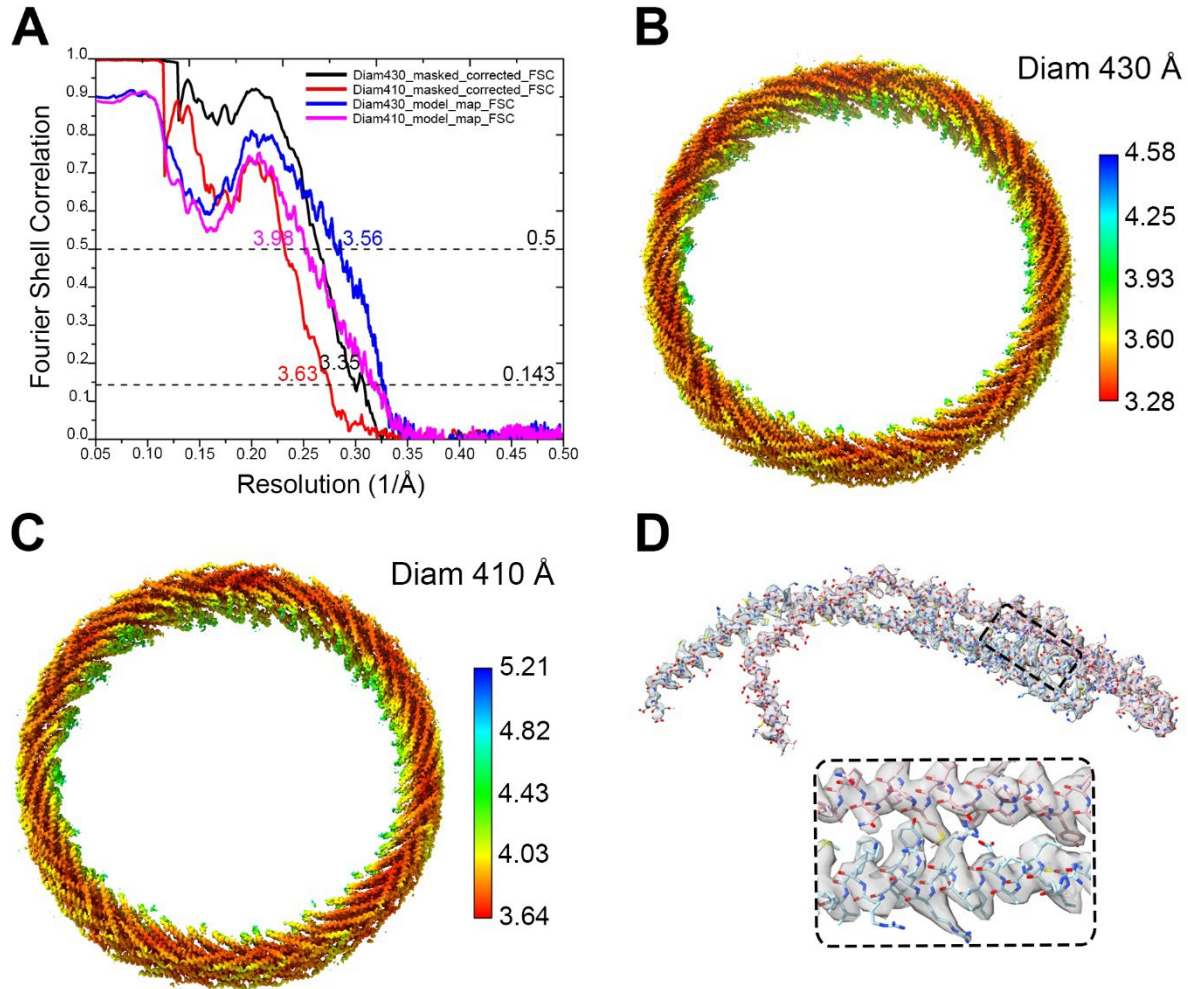
³ Institut Curie, Université PSL, Sorbonne Université, CNRS, Laboratoire Physico Chimie Curie,
Paris, France.



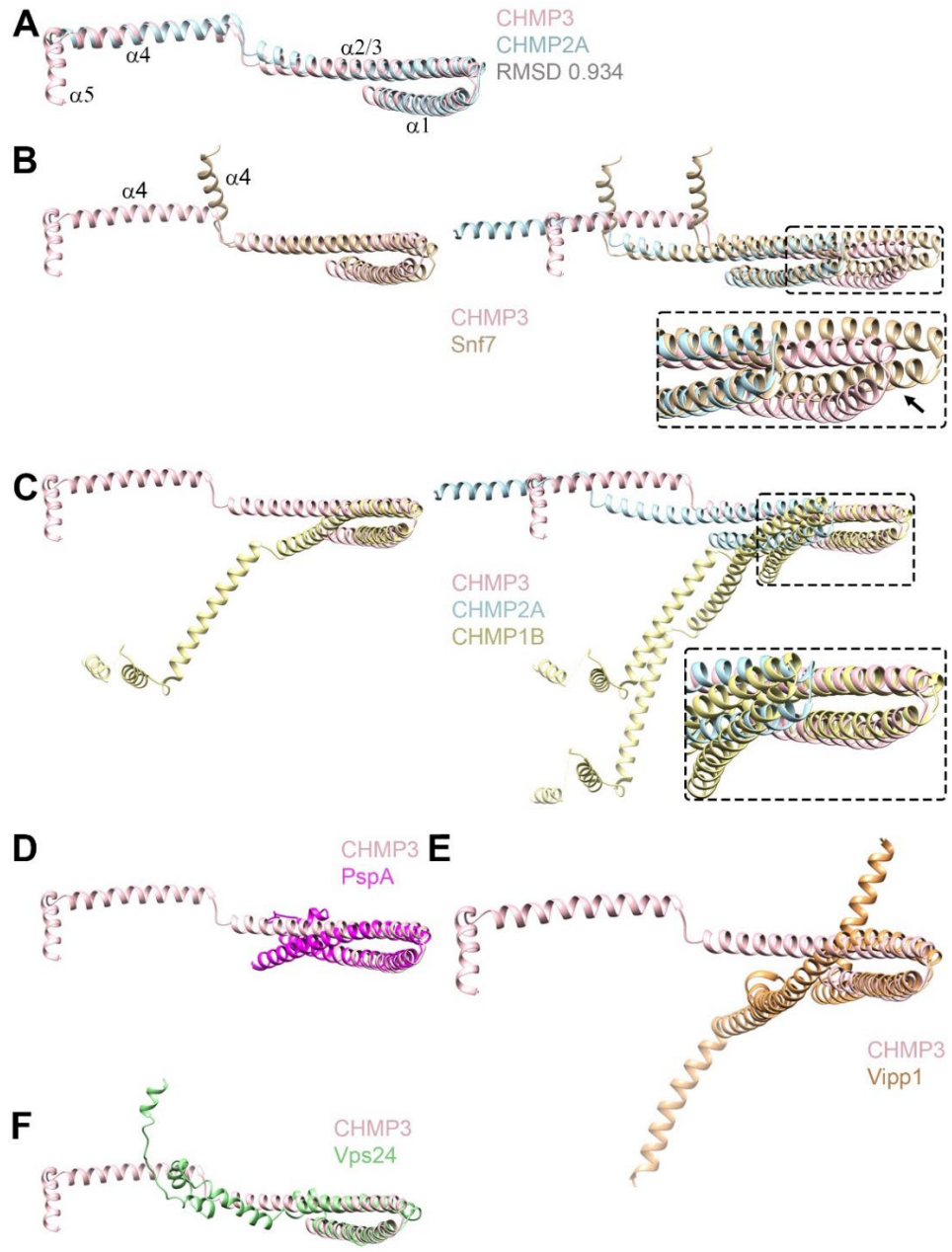
814 **Extended Data Fig.1: Cryo-EM data processing of CHMP2A-CHMP3 membrane-coated tubes and**
815 **helical symmetry analyses**
816 **(A)** Representative cryo-electron micrograph of CHMP2A-CHMP3 membrane tubes, with an arrow pointing
817 to the lipid bilayer. Scale bar, 50 nm.
818 **(B)** Selected 2D class averages of manually picked datasets, arranged according to the tube diameter
819 ranging from 380 to 490 Å as indicated.
820 **(C), (D)** Helical symmetry determination and representation of the elementary and biological helices for the
821 430 Å and 410 Å diameter tubes. Left panel, the sum of the 2D power spectra of segments corresponding
822 to one class-average show in both cases a maximum on or near the meridian corresponding to the pitch
823 (Bessel order $n=1$ for C1 helix; $n=2$ for C2 helix) instead of the axial rise, due to the large helical diameter
824 and possible inclusion of slightly out-of-plane tilted segments in the class-average. The left half of the sum
825 of the power spectra show the calculated position from helixplorer of the two first maxima of each Bessel
826 function corresponding to the determined symmetry. Middle panel, six asymmetric units (CHMP2A-CHMP3
827 dimers; in red) of the elementary helix are represented. The symmetry related protomers of the 430 Å
828 diameter are colored in light red.
829 **(C), (D)** Right panel, side view of the elementary helix with turns (red, yellow, green, blue and aqua) indicated
830 with a black dashed line. The grey dashed line follows one turn of the biological helix. The central grey line
831 (in C) highlights the C2 symmetry axis. Symmetry parameters of both the elementary and biological helices
832 are indicated.
833 **(E)** Central slices looking down the helical axis of the cryo-EM 3D reconstructions of the 430 and 410 Å
834 diameter tubes. The red arrows in the right zoom-in images indicate the density of the N-terminal region
835 prone to insert into the lipid bilayer.
836



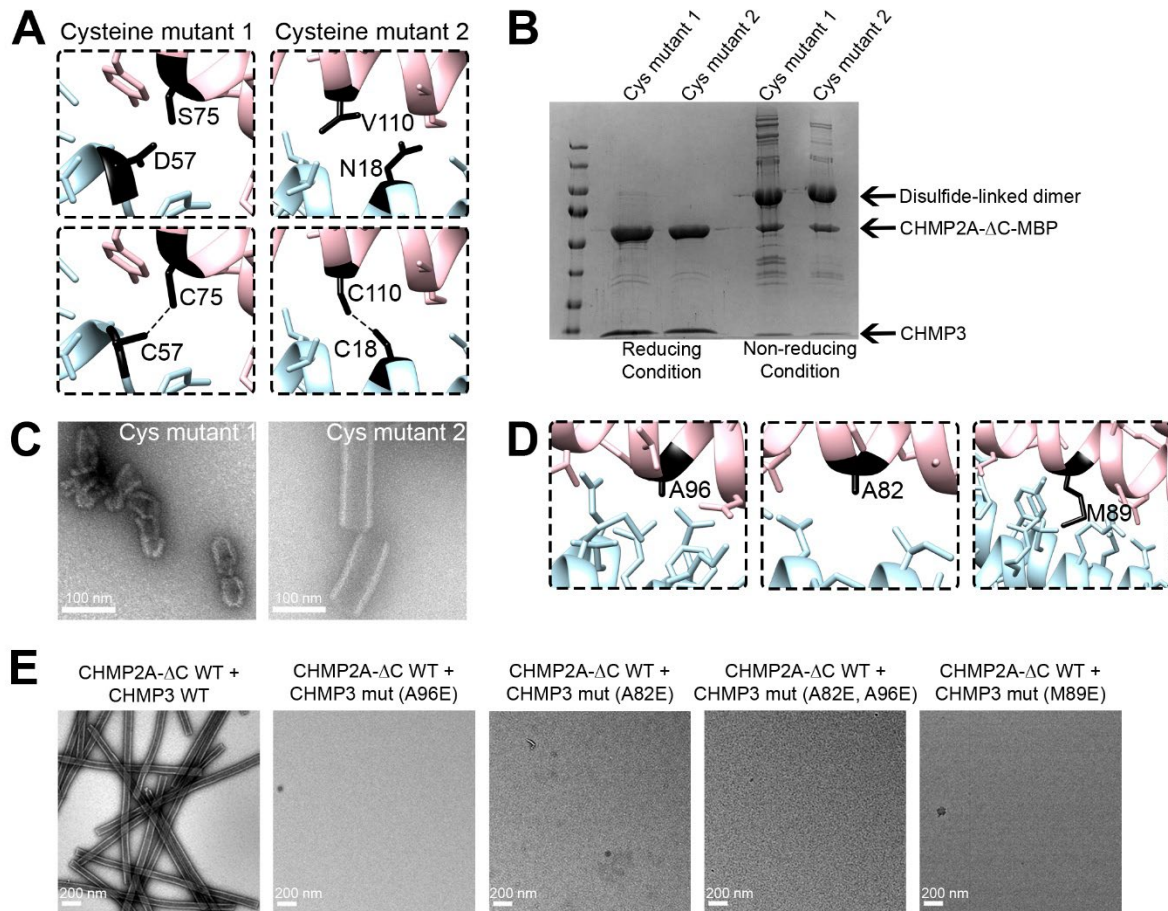
837
 838 **Extended Data Fig.2: Cryo-EM image processing workflow of 430 and 410 Å diameter tubes**
 839 **structure determination.**
 840 Basic image processing strategy used for helical 3D reconstruction and refinement of 430 and 410 Å
 841 diameter tubes is shown. Helical filaments were segmented and classified based on the tube diameter.
 842 Segment subsets were subjected to symmetry determination (<http://rico.ibs.fr/helixplorer/>) and initial 3D
 843 model generation in SPRING, followed by symmetry refinement and final 3D structure refinement in
 844 RELION. A complete description of the processing workflow is provided in 'Materials and Methods' section.
 845
 846



847
 848 **Extended Data Fig.3: 430 and 410 Å diameter tubes FSC curves, local resolution maps and atomic**
 849 **model fitting.**
 850 **(A)** FSC curves for the 430 Å (black) and 410 Å (red) diameter tube maps, with the resolutions at the FSC
 851 cut-off of 0.143 are indicated. Model versus map FSC curves, with the resolutions at the FSC cut-off of 0.5
 852 are indicated for the 430 Å (blue) and 410 Å (pink) diameter tube maps.
 853 Local resolution estimates are mapped onto the 430 Å **(B)**, and 410 Å **(C)** diameter tube cryo-EM density
 854 maps and the color keys (right) highlight the local resolution values in Å.
 855 **(D)** The refined atomic model of CHMP2A-CHMP3 dimer was fit into the corresponding cryo-EM density
 856 map of the 430 Å diameter tube. The inset (below) represents the zoomed-in view of the fitted model,
 857 indicating CHMP2A and CHMP3 helices and the corresponding map.
 858
 859



860
 861 **Extended Data Fig.4: Comparison of ESCRT-III open conformations highlights their versatile**
 862 **polymerization modes**
 863 **(A)** Ribbon diagram of C α superposition of CHMP2A and CHMP3 reveals an RMSD of 0.934 Å.
 864 **(B)** Ribbon diagram of C α superposition of CHMP3 with an Snf7 monomer (left panel) and with the
 865 homodimer (crystallographic dimer) (right panel), which indicates different hairpin interaction (arrow) for the
 866 second protomer and different orientations of Snf7 helix 4.
 867 **(C)** Ribbon diagram of C α superposition of CHMP3 and CHMP1B (left panel) and the superposition of the
 868 CHMP2A-CHMP3 heterodimer onto the CHMP1B homodimer (right panel) indicate the differences in helical
 869 hairpin stacking (zoom, right panel) and orientations of the C-terminal helical arms (helices 3 to 5).
 870 **(D)** Ribbon diagram of C α superposition of CHMP3 (pink) with PspA and **(E)** with Vipp1.
 871 **(F)** Ribbon diagram of C α superposition of CHMP3 with an intermediate Vps24 conformation that forms
 872 filaments on its own ⁴⁶.



873

874 **Extended Data Fig.5: Structure-based mutagenesis of CHMP2A-CHMP3 heterodimer formation and**
 875 **polymerization *in vitro*.**

876 (A) Close-up views of the pairs of residues (black) mutated to cysteine to induce the formation of disulfide-
 877 linked CHMP2A (light blue) - CHMP3 (pink) heterodimers upon polymerization.

878 (B) Cysteine cross-linking of the CHMP2A-CHMP3 heterodimer. Mutant CHMP2A_D57C was incubated
 879 with CHMP3_S75C and CHMP2A_N18C with CHMP3_V110C to induce polymerization as reported for wild-
 880 type CHMP2A and CHMP3³⁰. SDS-PAGE analysis showing that both CHMP2A_D57C-CHMP3_S75C and
 881 CHMP2A_N18C-CHMP3_V110C formed disulfide-linked dimers under non-reducing SDS PAGE
 882 conditions.

883 (C) Negative staining electron micrographs showing regular tube formation for CHMP2A_N18C-
 884 CHMP3_V110C (right), while CHMP2A_D57C-CHMP3_S75C (left) produced only shorter tubes. Scale bar,
 885 100 nm.

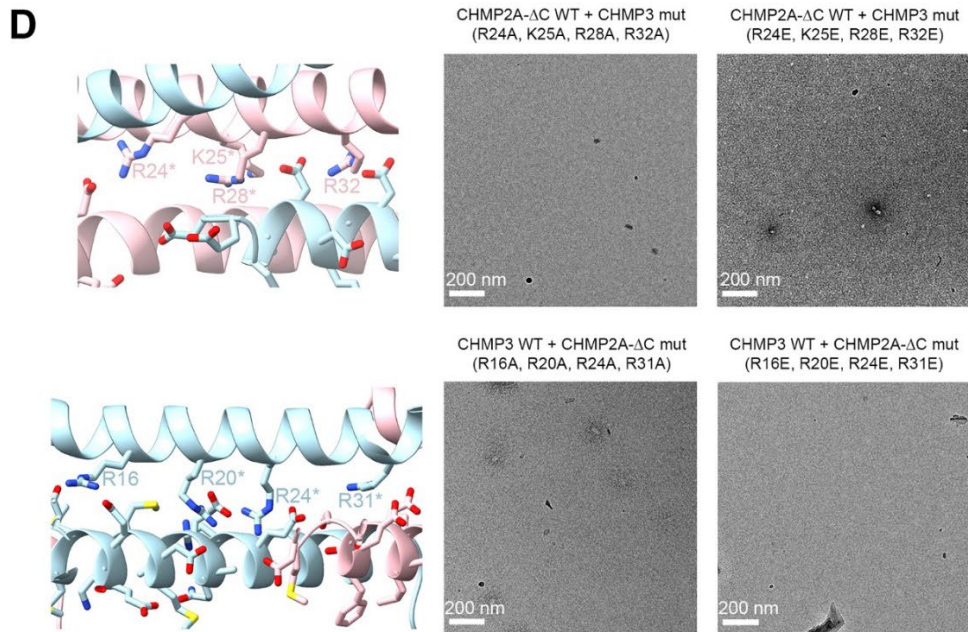
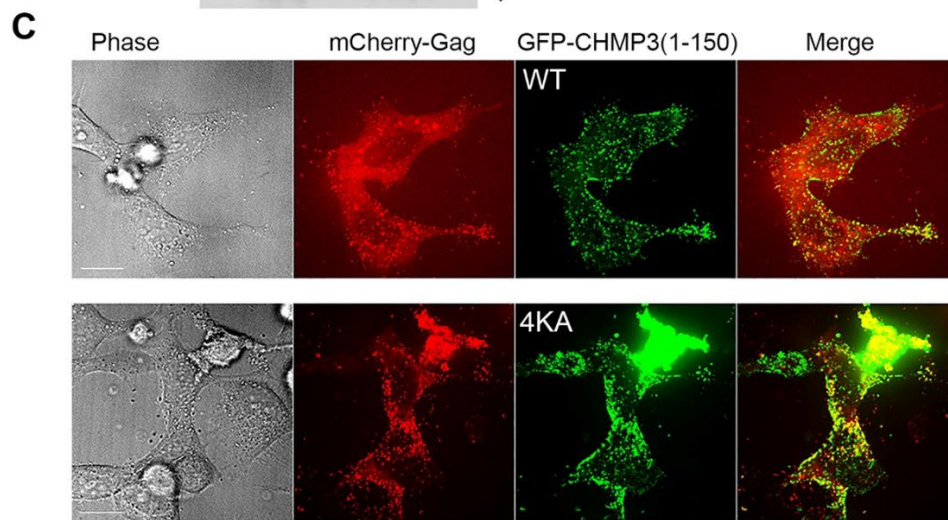
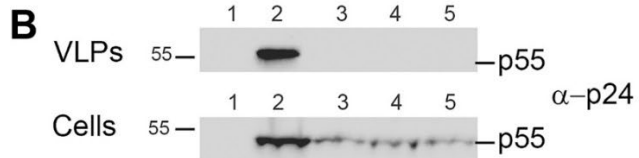
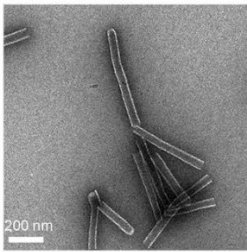
886 (D) Close-up views of the CHMP3 interface residues A96, A82 and M89E tested for heterodimer formation
 887 and polymerization.

888 (E) Negative staining electron micrographs of CHMP2A-CHMP3 wild-type and mutants (CHMP3_A96E,
 889 CHMP3_A82E, CHMP3_A82E_A96E and CHMP3_M89E) assemblies as indicated. Scale bar, 200 nm.

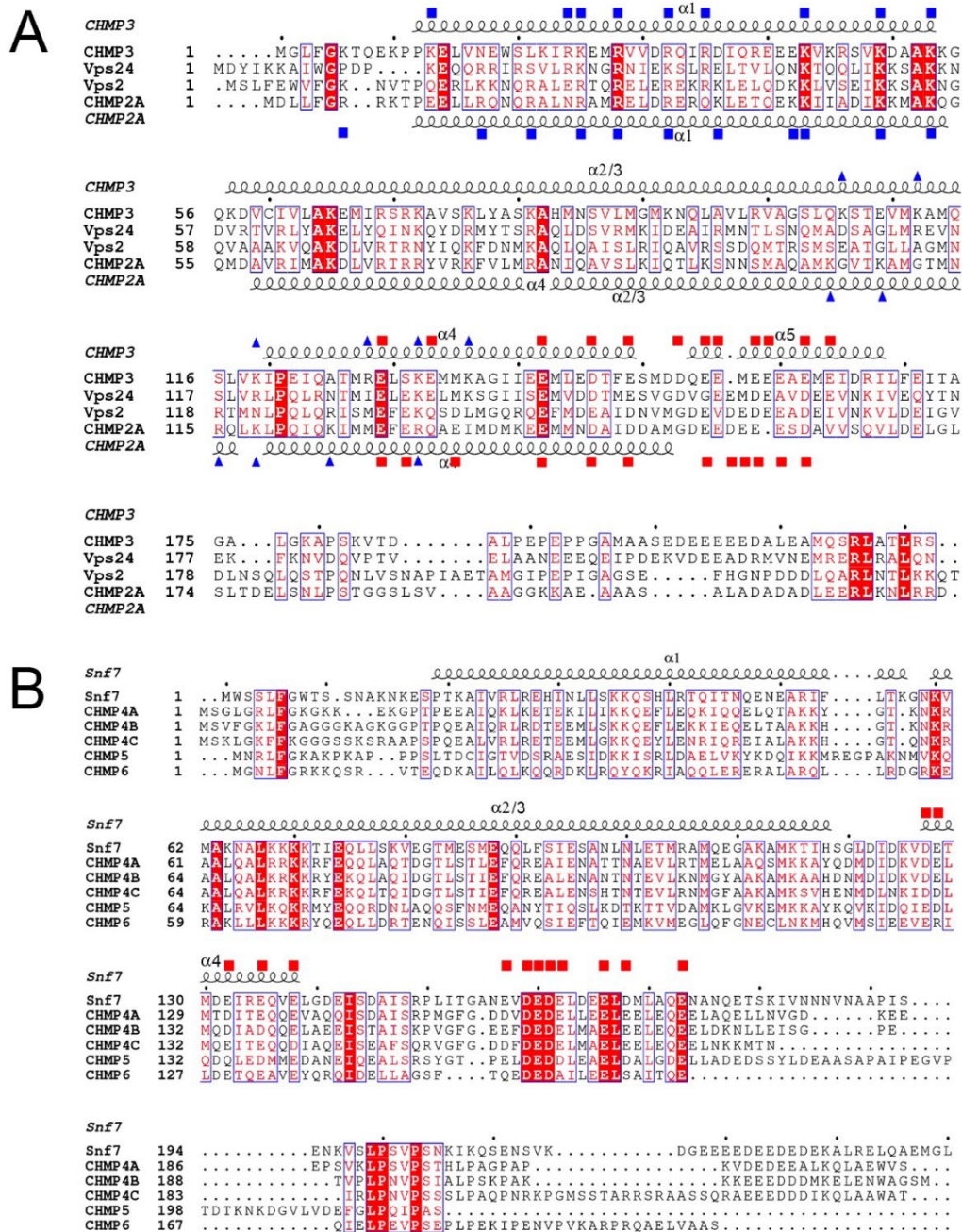
890

891

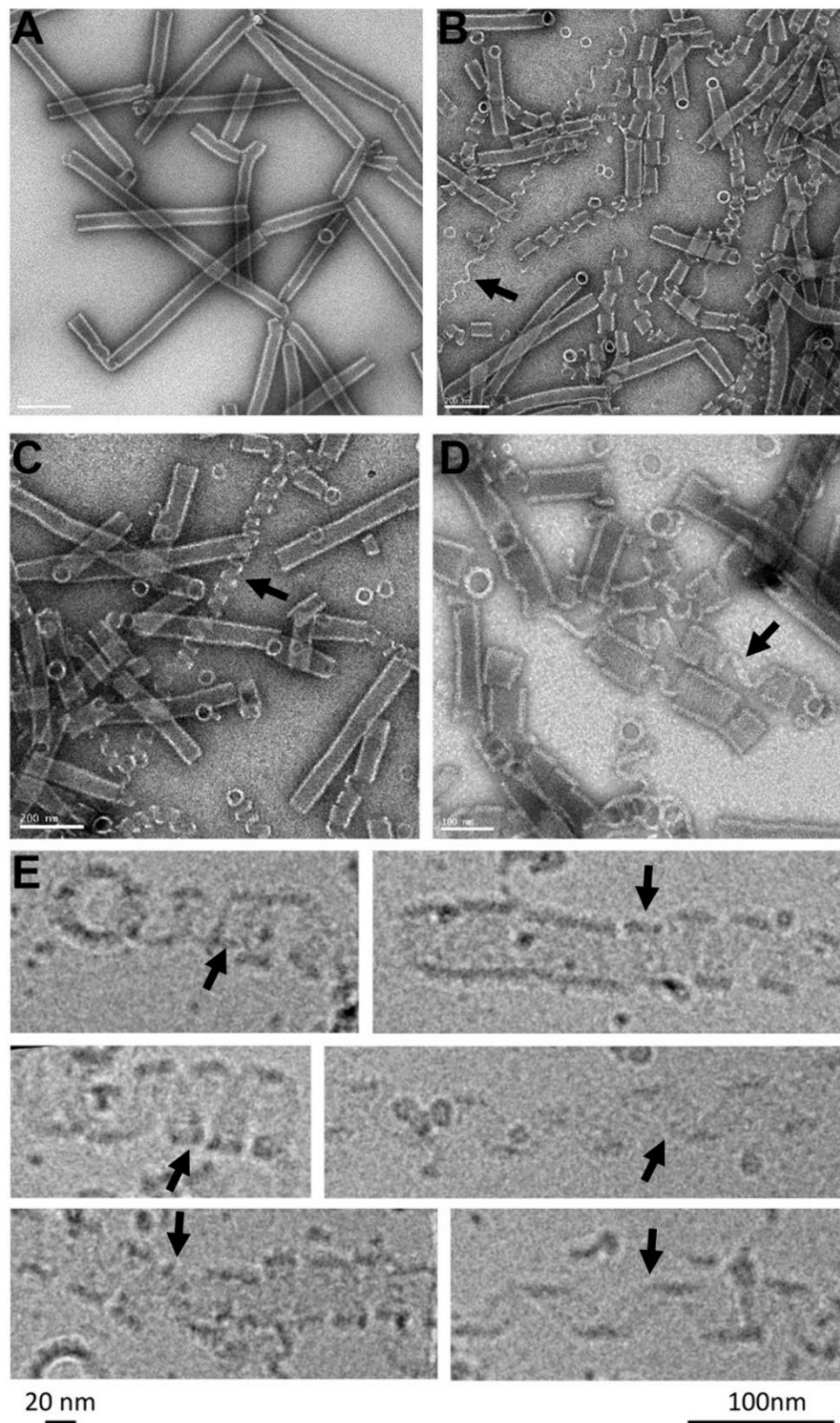
A CHMP2A-ΔC WT + CHMP3 mut
(K112A, K119A, K132A, K136A)



893 **Extended Data Fig.6: Structure-based mutagenesis of CHMP2A-CHMP3 polymer formation**
894 **(A)** Negative staining electron micrograph showing regular tube formation by CHMP2A-CHMP3_K112A,
895 K119A, K132A, K136A polymerization. Scale bar, 200 nm.
896 **(B)** The substitution of four basic residues in GFP-CHMP3(1–150) 4KA (K112A, K119A, K132A, K136A)
897 does not diminish its dominant-negative effect on HIV-1 budding. Western blot analyses of Gag released
898 from Gag expressing cells as Gag-VLPs (upper panel) and detection of Gag in total cell extracts (lower
899 panel): lane 1, Gag expression; lane 2, Gag and GFP-VPS4A E228Q expression; lane 3, Gag and GFP-
900 CHMP3(1-150) expression; lane 4, Gag and GFP-CHMP3(1-150) 4KA expression.
901 **(C)** Representative fluorescence images of HeLa cells transfected with Gag/mCherry-Gag and CHMP1(1-
902 150) or CHMP3(1-150)4KA. Cellular distribution of wild-type and mutant KA GFP-CHMP3(1–150) indicates
903 predominantly plasma membrane and intracellular localization as well as co-localization with mCherry-Gag.
904 Scale bar, 10 μ m.
905 **(D)** Negative staining electron micrographs showing no polymer formation of CHMP3 mutants (upper left
906 panel, close-up of a ribbon diagram illustrating the interface residues) R24A, K25A, R28A, R32A (upper
907 middle panel) and R24E, K25E, R28E, R32E (upper right panel) with CHMP2A. (Lower panel) CHMP2A
908 mutants (lower left panel, close-up of a ribbon diagram illustrating the interface residues) R16A, R20A,
909 R24A, R31A (lower middle panel) and R16E, R20E, R24E, R31E (lower right panel) did not polymerize with
910 CHMP3 *in vitro*. Scale bar, 200 nm.
911
912

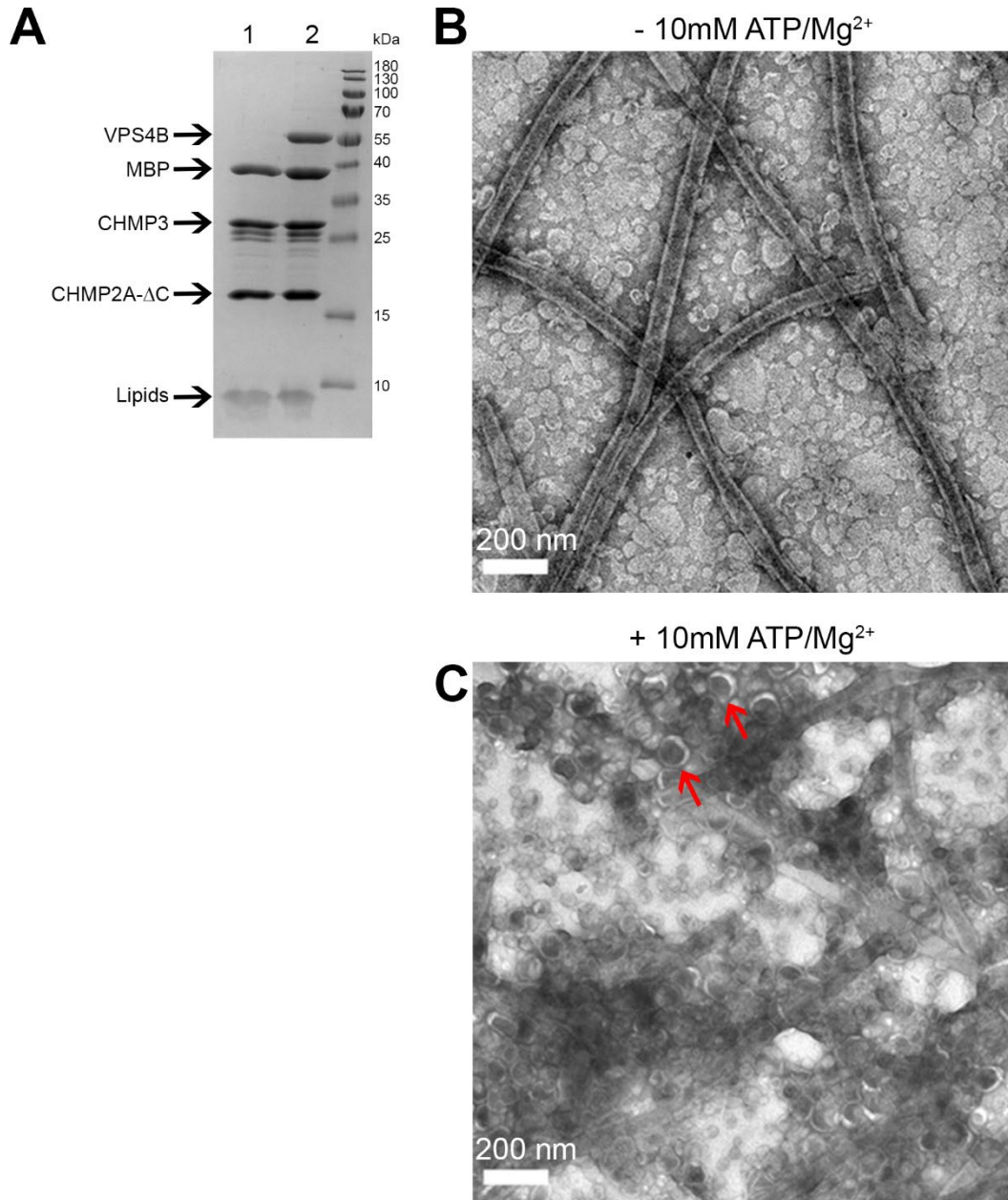


913
 914 **Extended Data Fig.7: ESCRT-III sequence alignment.**
 915 **(A)** Sequence alignment of CHMP3 (AF219226), *S. cerevisiae* Vps24 (QHB09957), *S. cerevisiae*
 916 Vps2 (P36108.2) and CHMP2A (NM_198426.3). Secondary structure elements are shown for
 917 CHMP3 above the sequence and for CHMP2A below the sequence alignment. Blue triangles
 918 indicate basic residues of CHMP3 (above) and CHMP2A (below) exposed at the membrane
 919 binding interface. Blue rectangles show basic residues and red squares conserved acidic residues
 920 exposed at the interface between filaments.
 921 **(B)** Sequence alignment of *S. cerevisiae* Snf7 (Z73197.1) and its secondary structure (pdb 5FD9),
 922 CHMP4A (NM_014169.5), CHMP4B (NM_176812.5) CHMP4C (NM_152284), CHMP5
 923 (NM_016410.6) and CHMP6 (NM_024591.5). Conserved acidic residues implicated in inter-
 924 filament interactions in the CHMP2A-CHMP3 polymer are indicated as red squares.



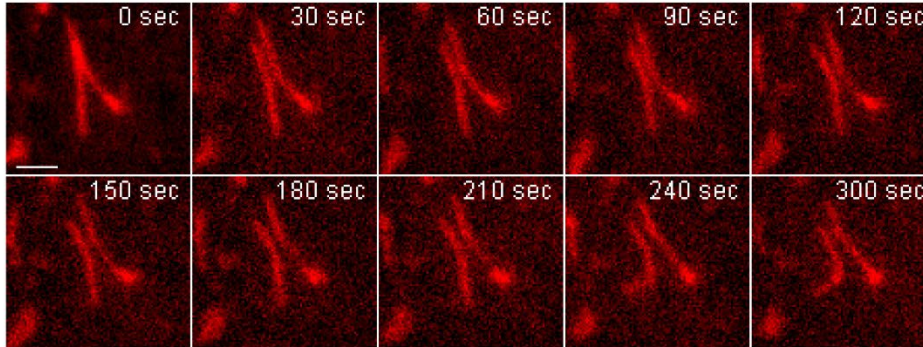
926

927 **Extended Data Fig.8: High ionic strength unwinds the CHMP2A-CHMP3 filaments.**928 **(A)** Negative staining electron micrographs showing CHMP2A-CHMP3 wild-type polymers after treatment
929 with 1M NaCl **(B, C)** and 1M KCl **(D)**.930 **(E)** Close-up of cryo-EM images shows unwinding of ~20 nm wide filaments corresponding to the six-start
931 helix observed in the structure. Single and multi-stranded unwound filaments are indicated by arrows.
932

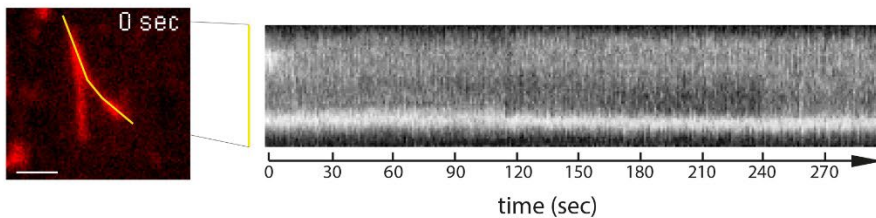


933
 934 **Extended Data Fig.9: Incorporation of VPS4B and ATP into CHMP2A-CHMP3 membrane tubes**
 935 **induces their disassembly.**
 936 **(A)** SDS-PAGE analyses of purified CHMP2A-CHMP3 polymers; lane 1, CHMP2A-CHMP3 polymers
 937 cleaved with TEV and coated with a lipid bilayer; lane 2 CHMP2A-CHMP3 polymers, TEV cleaved and
 938 incorporation of VPS4B prior to lipid bilayer coating.
 939 Negative staining electron micrographs of CHMP2A-CHMP3-VPS4B membrane-coated polymers before
 940 **(B)** and after **(C)** incubation with ATP and Mg²⁺. Red arrows point to membrane vesicles resulting from tube
 941 cleavage. Scale bar, 200 nm.
 942

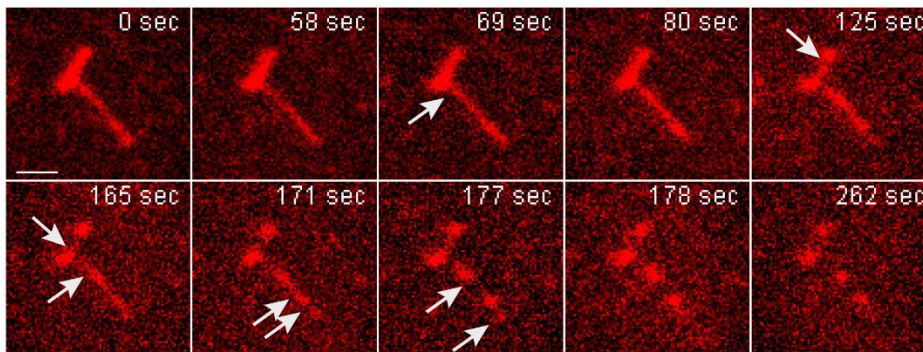
A + caged ATP



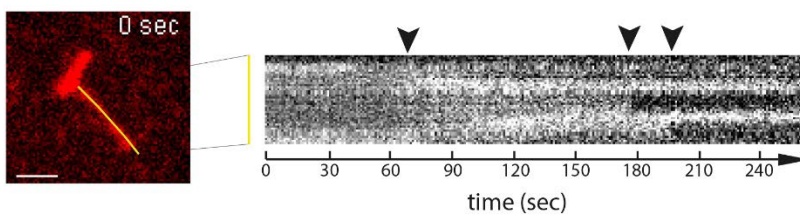
B



C + VPS4B and caged ATP

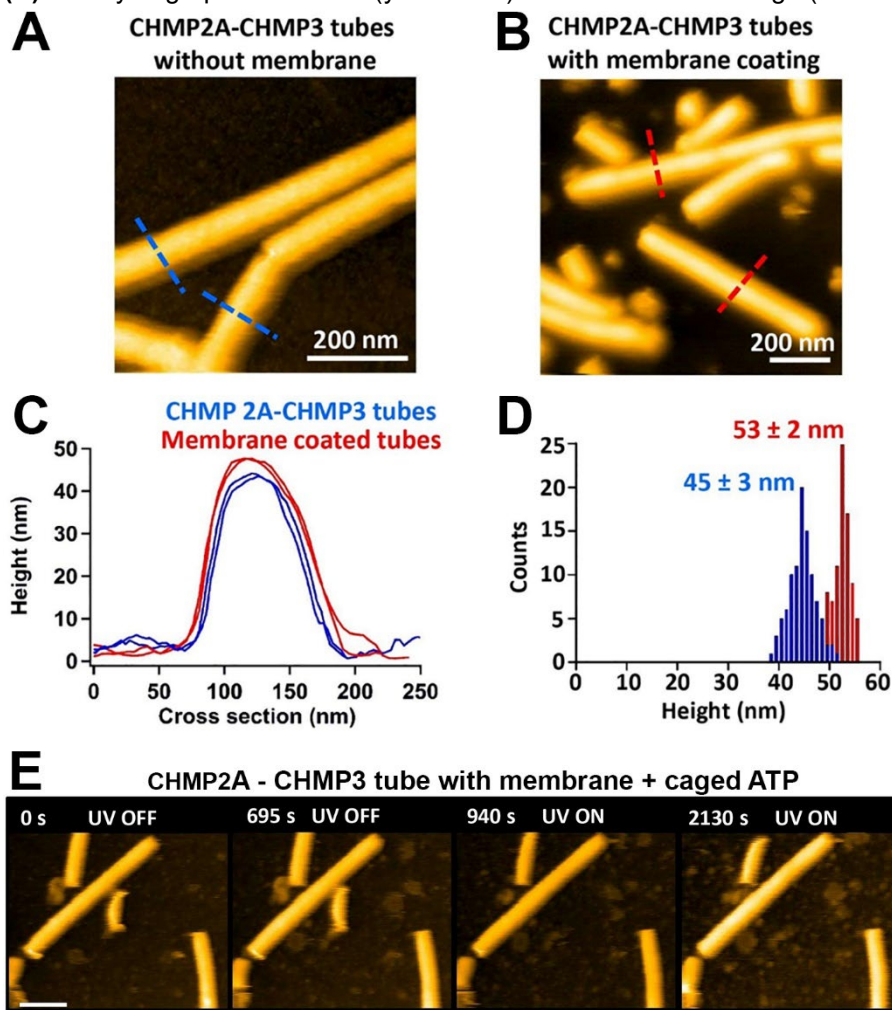


D



943
944 **Extended Data Fig.10: Imaging of VPS4B and ATP induced cleavage of CHMP2A-CHMP3 membrane**
945 **coated tubes.**
946 **(A)** A CHMP2A-CHMP3-caged ATP membrane coated tube was activated at 365 nm (30%, 100 ms) to
947 uncage ATP and imaged over 282s, which indicated that uncaging did not change the tube structure (movie
948 S3).
949 **(B)** The kymograph of the tube (yellow line) shows that the tube stays intact over the imaging time.
950 **(C)** Imaging of a CHMP2A-CHMP3-VPS4B-caged ATP membrane-coated tube following ATP uncaging
951 (365 nm, 30%, 100 ms) reveals cleavage of the tube at several sites over the imaging time (movie S5).
952 Scale Bar, 1 μ m.

953 (D) The kymograph of the tube (yellow line) indicates tube cleavage (arrows) over the imaging time.



954 **Extended Data Fig.11. Height distribution of CHMP2A-CHMP3 tubes with and without membrane-**
955 **coating.**

957 (A) AFM image of CHMP2A-CHMP3 tubes without membrane.

958 (B) AFM image of CHMP2A-CHMP3 tubes coated with membrane.

959 (C) Cross-section of AFM images of CHMP2A-CHMP3 in panel A (blue dotted line) and panel B (red dotted
960 line).

961 (D) Height histogram of CHMP2A-CHMP3 tubes with (red) and without (blue) membrane coating with
962 respect to the surface.

963 (E) Snapshots HS-AFM images of membrane-coated tubes loaded with 10 mM caged ATP taken with and
964 without UV irradiation. The UV was turned on from 700 s onwards. Scale bar, 200 nm.

965
966

967 **Movies**

968
969 **Movie 1: Fluorescence microscopy imaging of CHMP2A-CHMP3 membrane coated tubes.** A
970 CHMP2A-CHMP3-caged ATP membrane-coated tube was activated at 365 nm to uncage ATP and imaged
971 over 291s.

972 **Movie 2: Fluorescence microscopy imaging of CHMP2A-CHMP3 membrane coated tubes.** Another
973 dataset of CHMP2A-CHMP3-caged ATP membrane-coated tube activated at 365 nm 100 ms at each time
974 point to uncage ATP and imaged over 300s.

975 **Movie 3: Fluorescence microscopy imaging of CHMP2A-CHMP3 membrane coated tubes.** A
976 CHMP2A-CHMP3-VPS4B membrane-coated tube was activated at 365 nm to uncage ATP and imaged
977 over 251s.

978 **Movie 4: Fluorescence microscopy imaging of CHMP2A-CHMP3 membrane coated tubes.** Imaging of
979 a CHMP2A-CHMP3-VPS4B-caged ATP membrane-coated tube following ATP uncaging reveals a tube
980 fission followed by a shrinking event from both sides.

981 **Movie 5: Fluorescence microscopy imaging of CHMP2A-CHMP3 membrane coated tubes.** Another
982 dataset of CHMP2A-CHMP3-VPS4B-caged ATP membrane-coated tube following ATP uncaging (100 ms
983 at each time point) reveals cleavage of the tube at several sites over the imaging time.

984 **Movie 6: Fluorescence microscopy imaging of CHMP2A-CHMP3 membrane coated tubes.** Imaging of
985 a CHMP2A-CHMP3-VPS4B-caged ATP membrane-coated tube following ATP uncaging showing at 36s a
986 shrinking event from the end of a tube and at 51s a cleavage of the tube.

987 **Movie 7: HS-AFM imaging of CHMP2A-CHMP3 membrane-coated tubes.** HS-AFM movie of membrane-
988 coated CHMP2A-CHMP3 tubes loaded with 10 mM caged ATP, taken before and after UV (365 nm)
989 irradiation. Imaging time 5 seconds/frame.

990 **Movie 8: HS-AFM imaging of CHMP2A-CHMP3 membrane-coated tubes.** HS-AFM movie of membrane-
991 coated CHMP2A-CHMP3 tubes loaded with 5 μ M VPS4B and 10 mM caged ATP, taken without UV
992 irradiation. Imaging time 3 seconds/frame.

993 **Movie 9: HS-AFM imaging of CHMP2A-CHMP3 membrane-coated tubes.** HS-AFM movie of membrane-
994 coated CHMP2A-CHMP3 tubes loaded with 5 μ M VPS4B and 10 mM caged ATP, taken with 365 nm UV
995 irradiation. Imaging time 2 seconds/frame.

996

997

998

Extended Data Table 1 – Cryo-EM data collection, refinement and validation statistics

	Membrane-bound CHMP2A + CHMP3 (Tube Diameter 430 Å) (EMD-14630, PDB 7ZCG)	Membrane-bound CHMP2A + CHMP3 (Tube Diameter 410 Å) (EMD-14631, PDB 7ZCH)
Data collection and processing		
Magnification	130,000x	130,000x
Voltage (kV)	300	300
Electron exposure per frame (e ⁻ /Å ²)	0.96	0.96
Number of frames	25	25
Defocus range (μm)	0.5-1.5	0.5-1.5
Pixel size (Å)	1.052	1.052
Refined helical symmetry	54.37°, 2.74 Å	57.04°, 1.44 Å
Point group symmetry	C2	C1
Initial particle images (no.)	45,847	80,524
Final particle images (no.)	25,353	11,396
Map resolution (Å)	3.3	3.6
FSC threshold	0.143	0.143
Refinement		
Initial model used (PDB code)	<i>de novo</i>	<i>de novo</i>
Model resolution (Å)	3.6	4.0
FSC threshold	0.5	0.5
Map sharpening <i>B</i> factor (Å ²)	-96.57	-101.52
Model-to-map fit		
Correlation coefficient, CC (mask)	0.80	0.77
Model Composition		
Chains	22	22
Nonhydrogen atoms	27,148	27,148
Protein residues	3,366	3,366
<i>B</i> factor (Å ²)		
Protein	74.18	90.17
R.m.s. deviations		
Bond lengths (Å)	0.004	0.004
Bond angles (°)	0.758	0.762
Validation		
MolProbity score	1.86	1.89
Clashscore	15.23	21.23
Rotamer outliers (%)	0.00	0.00
Cbeta deviations (%)	0.00	0.00
Ramachandran plot		
Favored (%)	97.02	97.68
Allowed (%)	2.98	2.32
Disallowed (%)	0.00	0.00